Contents lists available at ScienceDirect

Tectonophysics

journal homepage: www.elsevier.com

Thermochronological constraints on the Cambrian to recent geological evolution of the Argentine passive continental margin

Sebastian Kollenz [a], Ulrich A. Glasmacher [a, *], Eduardo A. Rossello [b], Daniel F. Stockli [c], Sabrina Schad [a], Ricardo E. Pereyra [d]

[a] Institute of Earth Sciences, Heidelberg University, Im Neuenheimer Feld 234, 69120 Heidelberg, Germany
[b] Departamento de Ciencias Geológicas, Facultad de Ciencias Exactas y Naturales, Universidad de Buenos Aires, Ciudad Autónoma de Buenos Aires, Argentina
[c] Department of Geological Sciences, The University of Texas at Austin, 1 University Station C9000, Austin, TX 78712-0254, USA
[d] Universidad Nacional de Salta (UNSa), Av. Bolivia 5150, 4400 Salta, Argentina

ARTICLE INFO

Article history:
Received 27 February 2016
Received in revised form 8 November 2016
Accepted 14 November 2016
Available online xxx

Keywords:
Thermochronology
Exhumation history
Passive cPlease leave Passive Continental Margin with Capitel Letters!!ontinental margin
Sierras Australes
Sierras Septentrionales
Argentine

ABSTRACT

Passive continental margins are geo-archives that store information from the interplay of endogenous and exogenous forces related to continental rifting, post-breakup history, and climate changes. The recent South Atlantic passive continental margins (SAPCMs) in Brazil, Namibia, and South Africa are partly high-elevated margins (~ 2000 m a.s.l.), and the recent N-S-trending SAPCM in Argentine and Uruguay is of low elevation. In Argentine, an exception in elevation is arising from the higher topography (> 1000 m a.s.l.) of the two NW-SE-trending mountain ranges Sierras Septentrionales and Sierras Australes. Precambrian metamorphic and intrusive rocks, and siliciclastic rocks of Ordovician to Permian age represent the geological evolution of both areas. The Sierras Australes have been deformed and metamorphosed (incipient - greenschist) during the Gondwanides Orogeny. The low-temperature thermochronological (LTT) data (< 240 °C) indicated that the Upper Jurassic to Lower Cretaceous opening of the South Atlantic has not completely thermally reset the surface rocks. The LTT archives apatite and zircon still revealed information on the pre- to post-orogenetic history of the Gondwanides and the Mesozoic and Cenozoic South Atlantic geological evolution. Upper Carboniferous zircon (U-Th/He)-ages (ZHe) indicate the earliest cooling below 180 °C/1 Ma. Most of the ZHe-ages are of Upper Triassic to Jurassic age. The apatite fission-track ages (AFT) of Sierras Septentrionales and the eastern part of Sierras Australes indicate the South Atlantic rifting and, thereafter. AFT-ages of Middle to Upper Triassic on the western side of the Sierras Australes are in contrast, indicating a Triassic exhumation caused by the eastward thrusting along the Sauce Grande wrench. The corresponding t-T models report a complex subsidence and exhumation history with variable rates since the Ordovician. Based on the LTT-data and the numerical modelling we assume that the NW-SE-trending mountain ranges received their geographic NW-SE orientation during the syn- to post-orogenetic history of the Gondwanides.

1. Introduction

"Passive" continental margins (PCMs) are "first-order" archives of the Earth's surface that store information from the interplay of endogenous and exogenous forces related to continental rifting, breakup, sea-floor spreading, post-breakup, and climate changes during their evolution. Along strike the recent elevation of PCMs varies from high elevations (> 1000 m a.s.l.) parallel to the shore line to very low elevations (< 50 m a.s.l.). Causes of such strong variations in recent topography are still in debate (Bauer et al., 2010, 2013, 2015). From the coast to inland the topography of high elevated PCMs is usually structured as described by Bishop (2007): "The classic morphology of high-elevation PCMs consists of a coastal plain of varying width, backed by a steep, often wall-like escarpment and a low-relief plateau surface inland of the escarpment lip". Traditionally, recent escarpments have been interpreted as formed by endogenous forces during the early rifting stage and, thereafter, steadily retreated landward into the upland plateau surface by exogenic forces (Ollier, 1985; Kooi and Beaumont, 1994, 1996; Gallagher et al., 1998; Summerfield, 2000; Braun and van der Beek, 2004; Braun et al., 2006; Cogné et al., 2012; Sacek et al., 2012). Initial tectonic and surface uplift of the rift shoulders was interpreted to be caused by mantle and asthenospheric driven processes such as plume activity, asthenosphere upwelling, and melt intrusion during rifting (McKenzie, 1978; Wernicke, 1985; Kusznir et al., 1987; Kusznir and Ziegler, 1992; Ziegler and Cloetingh, 2004). Numerical modelling by Huismans and Beaumont (2002, 2003, 2007, 2008) clearly indicated that the strength of the lithosphere is important to the height of the topography of the rift shoulder. Certain type of lithospheric strength will not generate high topography during the rifting stage Huismans and Beaumont (2011, 2014). Recently, the concept of dynamic topography evolution is supporting the mantle driven surface activities but clearly indicated that the process is ongoing and not only related to the rifting stage (Moucha and Forte, 2011, Dávila and Lithgow-Bertelloni, 2013).

* Corresponding author.
Email address: ulrich.a.glasmacher@geow.uni-heidelberg.de (U.A. Glasmacher)

http://dx.doi.org/10.1016/j.tecto.2016.11.019
0040-1951/

The causes for the occurrence of high-elevated PCMs (> 1000 m) close to the recent coastline, e.g. in Brazil, long after ending of the active rifting stage (initial endogenous forces, Franco-Magalhães et al., 2010) are still a case of research (Bishop, 2007; Japsen et al., 2006; Hiruma et al., 2010; Cogné et al., 2012; Sacek et al., 2012; Karl et al., 2013; Green et al., 2013). In 2011, Osmundsen and Redfield (2011) published the hypothesis of a relationship between the gradient of crustal thinning and the evolution of the onshore seaward-facing escarpments. They showed that the highest recent escarpments and the most asymmetric recent margin morphology are located where the crystalline basement is tapering very sharply. In contrary, lower recent escarpments are situated on more gentle tapers (Osmundsen and Redfield, 2011).

Along the recent South Atlantic "passive" continental margin (SAPCM) the onshore topography varies significantly. Whereas the SAPCMs in Brazil, Namibia, and South Africa are partly high-elevated margins (~ 2000 m a.s.l.), the SAPCM in Argentine and Uruguay is in general of low elevation. The onshore part of the SAPCM in Argentine is characterized by a very even topography with elevations of up to 50 m a.s.l., in general. Nevertheless, two NW-SE trending mountain ranges (Fig. 1), the Sierras Septentrionales and Sierras Australes, truncate the low elevation by reaching exceptionally elevations of > 1.000 m a.s.l. The trending direction is nearly perpendicular to the trending of the Argentine SAPCM and the recent offshore spreading ridge.

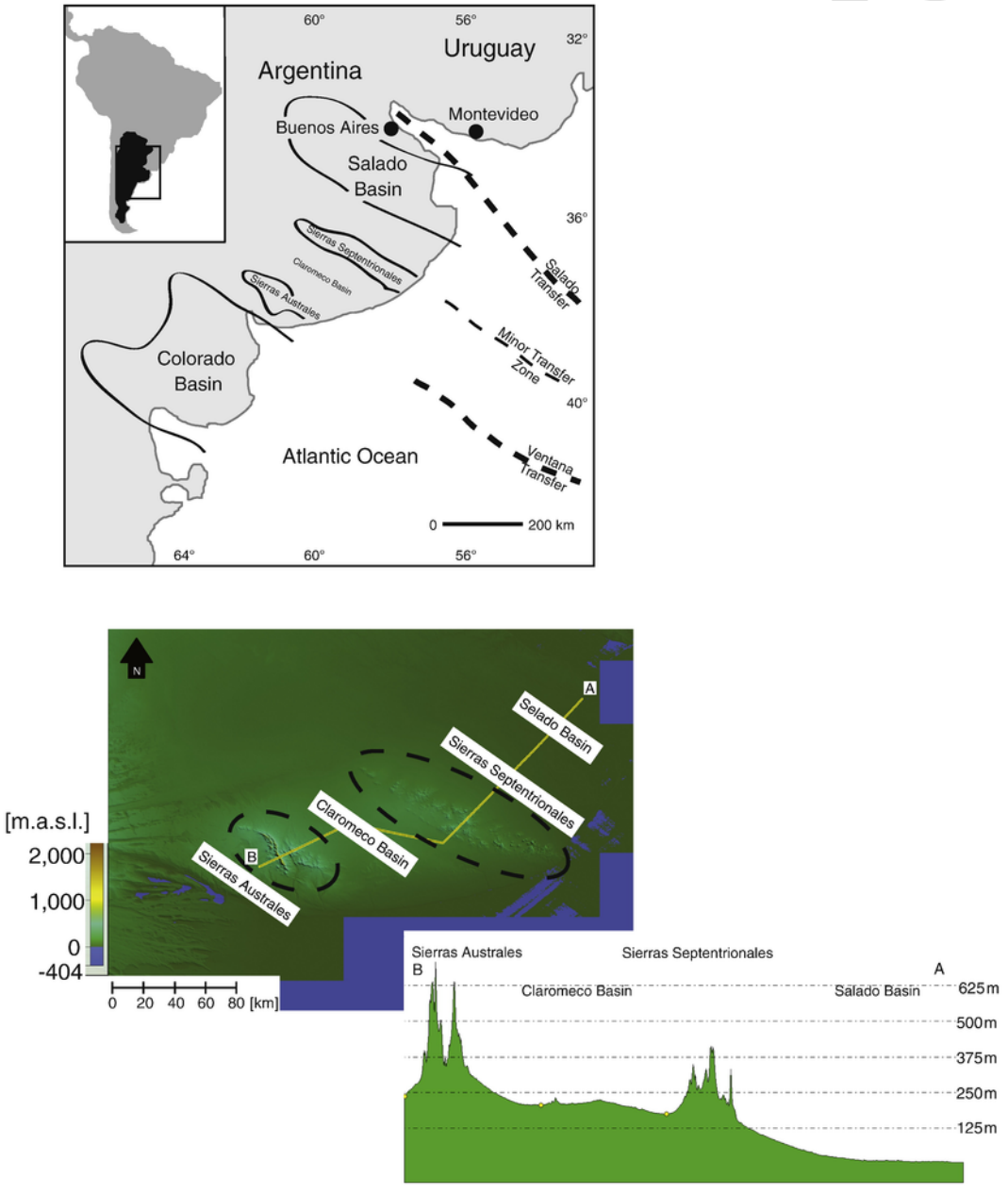

Fig. 1. Location map of the Sierras Septentrionales, the Sierras Australes and the basin structures of the area (modified from Tomezzoli, 2001), combined with the margin segmentation by transfer zones (Franke et al., 2007). In addition, DEM 90 m images with a cross-section through the research area are displayed.

Our research focused on the following questions:

- What are the causes for the perpendicular trending of the mountain ranges in relation to the Argentine SAPCM?
- Did the Argentine SAPCM ever evolved to a high-elevation margin during or shortly after the rifting stage?
- If the Argentine SAPCM has had a high topography was it fast retreated or did it subside, thereafter?
- Did differentiated exhumation occur and is it controlled by pre-, syn-, and/or post-rift endogenic and exogenic forces.

Quantification of the rate at which landforms adapt to changing tectonic, and climate forces on a broad time scale uses data revealed by low-temperature thermochronology (LTT). LTT-dating techniques, such as fission-track (FT) and (U-Th-Sm)/He (He) dating of apatite and zircon provide information on the cooling and heating history of rocks. Using the geological published knowledge and the annealing and diffusion kinetics allows determining the t-T evolution of crustal segments by numerical modelling. Assumptions related to the geothermal gradient and the surface temperature over time provide the possibility to calculate the exhumation history of the crustal segments. Comparing the exhumation rates with the sedimentation rates of adjacent basins and assuming a lag time for the transportation of sediments from their source region to the basins allows judging the erosion rates. All this data and interpretation lead to answer the above described research questions.

2. Geological setting and topography

The area of investigation consists of two NW-SE trending mountain ranges, the Sierras Septentrionales (Tandil Hills) and the Sierras Australes (Ventana Hills). Both mountain ranges (Fig. 1) are surrounded and separated by three basins: Northeast of the Sierras Septentrionales the Salado basin, between the Sierras Septentrionales and Sierras Australes the intracratonic Claromecó basin, and southwest of the Sierras Australes the Colorado basin. Both, the Salado basin and the Colorado basin extend from onshore to offshore and are trending partly perpendicular to the continental margin and recent spreading axes.

2.1. The Salado basin

The Salado basin, a graben-like basin, is bound by NW-SE and N/S trending faults (Zambrano and Urien, 1970; Introcaso and Ramos, 1984) and is filled with up to 6500 m thick Mesozoic and Cenozoic volcanic (Upper Jurassic), siliciclastic and evaporitic sedimentary sequences (Crovetto et al., 2007; CarolCarol et al. 2010, 2010; Fig. 2A). The transition of the Salado basin towards the Sierras Septentrionales is not well defined and its geological nature is still in discussion (Franke et al., 2007; Zambrano and Urien, 1970; Perez-Diaz and Eagles, 2014). Due to post-depositional faulting the Precambrian metamorphic and granitoid basement emerges to the surface at some locations (e.g. the Martin Garcia Island) (Crovetto et al., 2007). In contrast to the Precambrian basement lithology of the Colorado basin, the basement lithology of the Salado basin is similar to the Uruguayan basement lithology and is overlain by upper Jurassic to lower Cretaceous basaltic flows of the Serra Geral Formation (Zambrano and Urien, 1970). 3500 m thick siliciclastic “Rio Salado Formation” of Upper Cretaceous age dominated by an intercalation of cross-bedded sand- silt-, and claystones overlie the Serra Geral Formation. The “Rio Salado Fm.” is overlain by the “General Belgrano Formation”, a 890 m thick continental intercalation of claystones, and sandstones with conglomerates. Zambrano (1974) argues for an Upper Cretaceous age but Bracaccini (1980) discussed a lower Palaeogene age of the sequence. Marine clay- and siltstones with anhydrite and gypsum of the Parana formation occur at the top of the sedimentary sequence (Introcaso and Ramos, 1984).

2.2. The Sierras Septentrionales

The stratigraphic ages in the Sierras Septentrionales reach from Palaeoproterozoic crystalline basement (Buenos Aires Complex) to Silurian siliciclastic sequence (Balcarce Formation) (Cingolani, 2011; Figs. 2B and 3A). Calc-alkaline granitoids, granulite-facies orthogneisses, amphibolite-facies schists, marbles, and migmatites are the main lithologies of the crystalline basement (Dalla Salda, 1975; Cingolani, 2011, Hartmann et al., 2002). Deformation and metamorphism are related to continental collision between 2.25 Ga - 2.08 Ga (Cingolani, 2011). Formation or reactivation of one of the mega-shear zones occur between 2.0 and 1.6 Ga (D'Angiola et al., 1992). Neoproterozoic conglomerates and sandstones of the Sierras Bayas Group discordantly overlay the metamorphic crystalline basement. The Neoproterozoic Sierras Bayas Group comprises diamictites, shales, quartz-arenites, dolostones, and micritic limestones and is discordantly overlain by the Cerro Negro Formation (Zimmermann et al., 2011). The Neoproterozoic Cerro Negra Formation consists of a basal phosphorite and chert breccia, marls, shales, and shale/sandstone heterolithic facies (Poiré and Gaucher, 2009), and is overlain by the siliciclastic (quartz-arenites, kaolinitic shales) Balcarce Formation of Ordovician to Silurian age (Poiré et al., 2003). Detrital zircon U-Pb ages indicated - in order of decreasing importance - Palaeoproterozoic, Achaean and Mesoproterozoic source rocks for the sedimentary sequence of Neoproterozoic age (Rapela et al., 2007; Gaucher et al., 2008; Cingolani, 2011).

2.3. Claromecó Basin

The NW-SE trending Claromecó Basin comprises a long lasting sedimentary history (> 9000 m of sedimentary rocks) from Proterozoic to Cenozoic with differentiated subsidence and inversion rates (Kostadinoff and Font, 1985; Kostadinoff, 1993).

The sedimentary sequences of the Carboniferous to Permian Pillahuinco Group are composed of arkoses and subarkoses with volcanic clasts. These sedimentary units are described as a synorogenic molasse foreland sequence (Alessandretti et al., 2013). The Pillahuinco Group consist of the Sauce Grande Formation, the Piedra Azul Formation, the Bonete Formation and the Tunas Formation.

2.4. The Sierras Australes

The Sierras Australes is a typical fold-and-thrust belt with wrench faults, which has been structurally formed during the Carboniferous to Upper Permian Gondwanides orogeny (Fig. 3B; Keidel, 1916, 1921; Ramos et al., 2013). Similarly, the Cape Fold Belt has been formed during the same orogeny (Keidel, 1916, 1921). Precambrian basement rocks of similar metamorphic and intrusion ages (Rapela et al., 2003), very similar Palaeozoic lithology and biostratigraphy (Fig. 2C; Harrington, 1955; Benedetto, 2010), and similar glacial deposits of Carboniferous to Permian age (Keidel, 1913, Lopez-Gamundi and Rossello, 1998) characterize both fold-and-thrust belts. The Precambrian crystalline basement was intruded by S-type granites in Neoproterozoic time (607 ± 5 Ma, U-Pb zircon age), and A-type granite during the Cambrian (531–524 Ma). In the Upper Permian, folding of the Palaeozoic quartzite's and sandstones (Sierras Australes, especially the Curamalal and Ventana Group) lead to the formation of

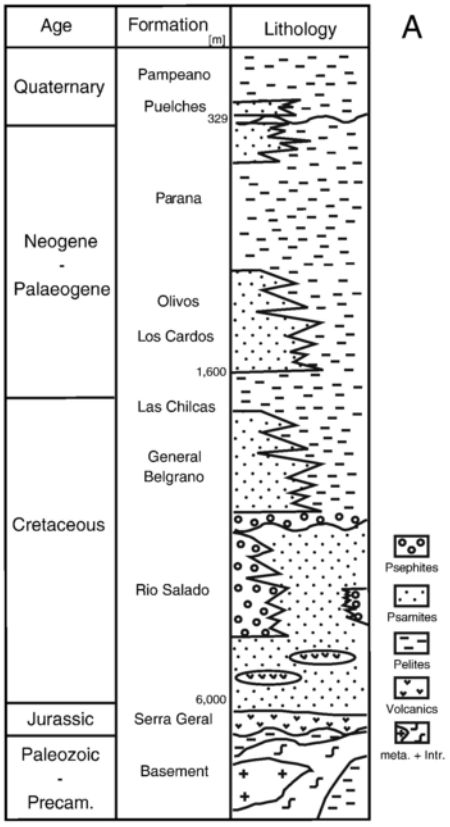
A
Age
Formation [m]
Lithology
Quaternary
Pampeano
Puelches
329
Neogene - Palaeogene
Parana
Olivos
Los Cardos
1,600
Las Chilcas
Cretaceous
General Belgrano
Rio Salado
6,000
Jurassic
Serra Geral
Paleozoic - Precam.
Basement
Psephites
Psarnites
Pelites
Volcanics
meta. + Intr.

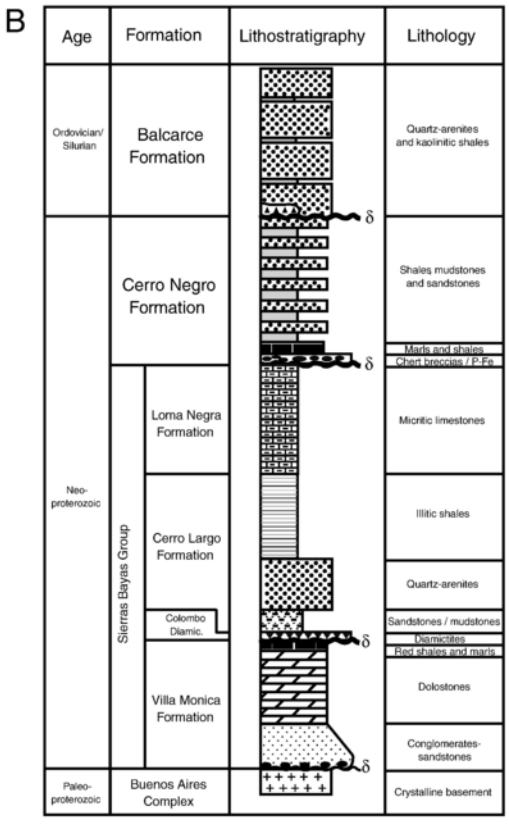
B
Age
Formation
Lithostratigraphy
Lithology
Ordovician/ Silurian
Balcarce Formation
Quartz-arenites and kaolinitic shales
Cerro Negro Formation
Shales, mudstones and sandstones
Marls and shales
Chert breccias / P-Fe
Neo-proterozoic
Sierras Bayas Group
Loma Negra Formation
Micritic limestones
Cerro Largo Formation
Illitic shales
Quartz-arenites
Colombo Diamic.
Sandstones / mudstones
Diamictites
Red shales and marls
Villa Monica Formation
Dolostones
Conglomerates-sandstones
Paleo-proterozoic
Buenos Aires Complex
Crystalline basement

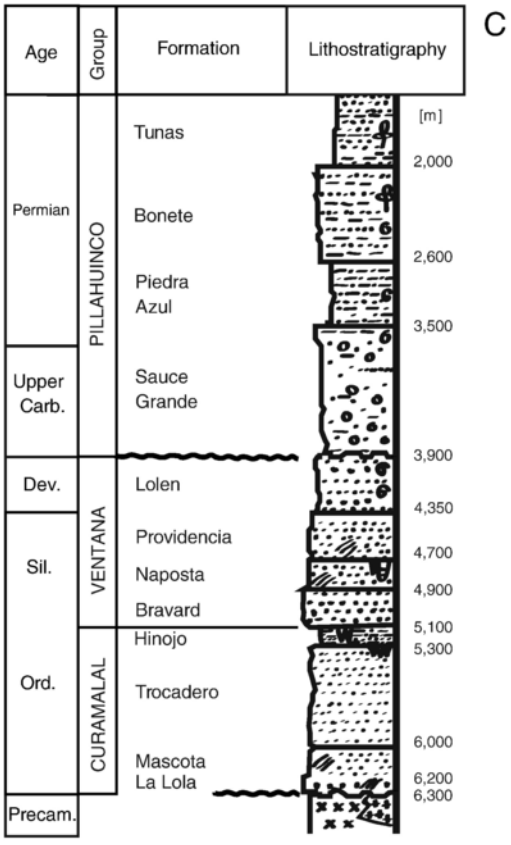
C
Age
Group
Formation
Lithostratigraphy
[m]
Permian
PILLAHUINCO
Tunas
2,000
Bonete
2,600
Piedra Azul
3,500
Upper Carb.
Sauce Grande
3,900
Dev.
VENTANA
Lolen
4,350
Sil.
Providencia
4,700
Naposta
4,900
Bravard
5,100
Hinojo
5,300
Ord.
CURAMALAL
Trocadero
6,000
Mascota
6,200
La Lola
6,300
Precam.

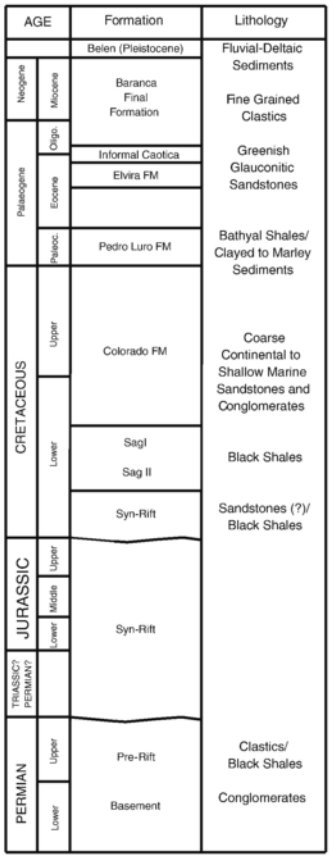
D
AGE
Formation
Lithology
Belen (Pleistocene)
Fluvial-Deltaic Sediments
Neogene
Miocene
Baranca Final Formation
Fine Grained Clastics
Olig.
Informal Caotica
Greenish Glauconitic Sandstones
Palaeogene
Eocene
Elvira FM
Paleoc.
Pedro Luro FM
Bathyal Shales/ Clayed to Marley Sediments
CRETACEOUS
Upper
Colorado FM
Coarse Continental to Shallow Marine Sandstones and Conglomerates
Lower
Sag I
Sag II
Black Shales
Syn-Rift
Sandstones (?)/ Black Shales
JURASSIC
Upper
Middle
Lower
Syn-Rift
TRIASSIC? PERMIAN?
PERMIAN
Upper
Pre-Rift
Clastics/ Black Shales
Lower
Basement
Conglomerates

chevron or concentric folds with flexural slip movement. The fold axes are trending NW/SE with local culminations (Cobbold et al., 1986). Von Gosen et al. (1990) reported a tectonic and thermal overprint of the basement rocks and the Palaeozoic cover in the middle to upper Permian. They described the P-T environment as anchizonal to lower-greenschist facies due to recrystallization and quartz deformation and most of all due to the crystallization of illite. At different locations within the Sierras Australes K/Ar-ages of illite vary between 282 ± 3 Ma, and 260 ± 3 Ma. The K/Ar-ages are interpreted as illite formation ages.

The Sauce Grande wrench fault with a western thrust component separates the mountain range into a western and an eastern crustal segment with variable degree of deformation and metamorphism.

The Western crustal segment consists of a highly deformed strongly cleaved (folding, reverse faulting) lower-greenschist facies (> 300 °C) siliciclastic rock sequence (> 2300 m) of Ordovician to Devonian age (Curamalal and Ventana Group; von Gosen et al., 1991). Along the Sauce Grande wrench the lower-greenschist facies Palaeozoic sedimentary rocks were overthrusted by the upper diagenesis to very low-grade (anchizonal) siliciclastic rocks of the Upper Carboniferous to Permian Pillahuinco Group.

In the low-grade metamorphic Eastern area, the Upper Carboniferous to Permian siliciclastic rocks of the Pillahuincó Group are slightly deformed and reach upper diagenesis to very low grade metamorphic conditions. Deformation and remagnetization occurred in early Permian time (Tomezzoli and Vilas, 1999; Tomezzoli, 2001).

Southwest of the Sierras Australes Mountains within the Precambrian basement the Lopez Lecube syenite occurs. The intrusion age of 258 ± 2 Ma was determined by zircon U–Pb SHRIMP dating technique (Pankhurst et al., 2006). K/Ar dating of hornblende revealed a Permian to Triassic cooling age of 245 ± 12 Ma (Rossello et al., 1997).

2.5. The Colorado Basin

Southwest of the Sierras Australes range, the NW-SE trending Colorado Basin is characterized by an on- and offshore part with the basin axis trending partly perpendicular to the NE-SW direction of the "passive" continental margin (Bushnell et al., 2000; Pángaro and Ramos, 2012; Autin et al., 2013, 2015). The geological evolution comprises Permian conglomerates, sandstones, and black shales as the oldest known lithostratigraphic units (Fig. 2D; Fryklund et al., 1996; Bushnell et al., 2000; Vayssaire et al., 2007). The Triassic and Jurassic geological evolution is not recorded within the sedimentary rock column so far. In addition, it is unknown if Triassic and/or Jurassic sedimentary units were deposited and eroded before the deposition of Lower Cretaceous sandstones and black shales. Continuous sedimentation of coarse continental to shallow marine conglomerates, sandstones, and black shales represent the Lower and Upper Cretaceous (Colorado Fm). Subsidence of the Colorado basin in Cretaceous time is interpreted as caused by thermal and localized tectonic subsidence (Loegering et al., 2013). A shallow marine environment with the formation of shales, marls, marly shales, siltstones, and glauconitic sandstones characterizes the Palaeogene and Neogene geological evolution. During the Pleistocene and Holocene part of the Colorado basin was filled with fluvial to deltaic siliciclastic sediments. The accumulated thickness of the sedimentary record varies within the basin and can reach up to 16 km. Since the Cretaceous the basin architecture was redefined by differentiated tectonic activity causing activation and reactivation of normal faults systems and transform fault systems (Loegering et al., 2013).

2.6. Topography

The moderate topography of the Pampean Flat (altitudes between 0 and 50 m) is disturbed by the two mountain ranges Sierras Septentrionales and Sierras Australes (Fig. 1B). Smooth hills (350–400 m a.s.l.) surrounded by plains and grasslands characterize the topography of the Sierras Septentrionales. The Claromecó basin between both lower mountain ranges reaches altitudes of about 200 to 250 m a.s.l. The Cerro Ventana (1184 m a.s.l.) and the Cerro Tres Picos (1239 m a.s.l.) are the highest hills of the Sierras Australes. The significant difference in elevation between both mountain ranges is caused by the differences in lithologies. The highest hills in the Sierras Australes consist of weathering resistant quartzites of the Ordovician-Silurian Balcarce formation. Furthermore, the hills of the Sierras Australes show steep scarp slope in comparison to the Sierras Septentrionales.

3. Methods

Thermochronological methods, such as (U-Th-Sm)/He and fission-track (FT) dating, are based on the radioactive decay, the production of isotopic daughter products, and linear crystal defects, and the subsequent, thermally controlled retention of the decay products. Due to the thermal sensitivity of thermochronometers, thereof revealed ages provide information about the cooling history of the rock, rather than the crystallization ages of its minerals (although in some cases they do record crystallization ages as well).

To resolve the thermal and exhumation/erosion history of the Argentine passive continental margin, zircon and apatite fission-track (AFT, ZFT, respectively), and zircon and apatite (U-Th-Sm)/He analyses (AHe, ZHe, respectively) were performedPlease introduce in the text (Tables 1 - 6). Whenever possible all thermochronometers were applied to the same sample, allowing a more robust evaluation of the spatial and temporal cooling of the samples. Numerical modelling was used to determine the cooling histories of individual samples and trace their exhumation though the upper crust.

Twenty-one samples were processed with 14 samples yielding enough apatite and zircon grains for the analytical work. The majority of samples were taken from the Sierras Australes, 3 samples from the Sierras Septentrionales, and one from the border of the Claromecó basin. The sampled lithologies reach from Precambrian metamorphic basement up to the Permian sandstones of the Tunas formation (Table 1).

3.1. Fission-track dating

Information on the thermal history of apatite is stored in two archives: the etch pit areal density at an artificially polished internal surface, and the length distribution of horizontal confined tracks (Laslett et al., 1987; Green et al., 1986; Wagner and Van den haute,

Fig. 2. A) Stratigraphy of the Salado basin (Carol et al., 2010). B) Stratigraphy of the Sierras Septentrionales with corresponding depositional sequences (Poiré et al., 2003; Poiré and Gaucher, 2009). C) Stratigraphy of the Sierras Australes fold belt (redrawn after Buggisch, 1987). D) Stratigraphic record of the Colorado basin (modified after Vayssaire et al., 2007).

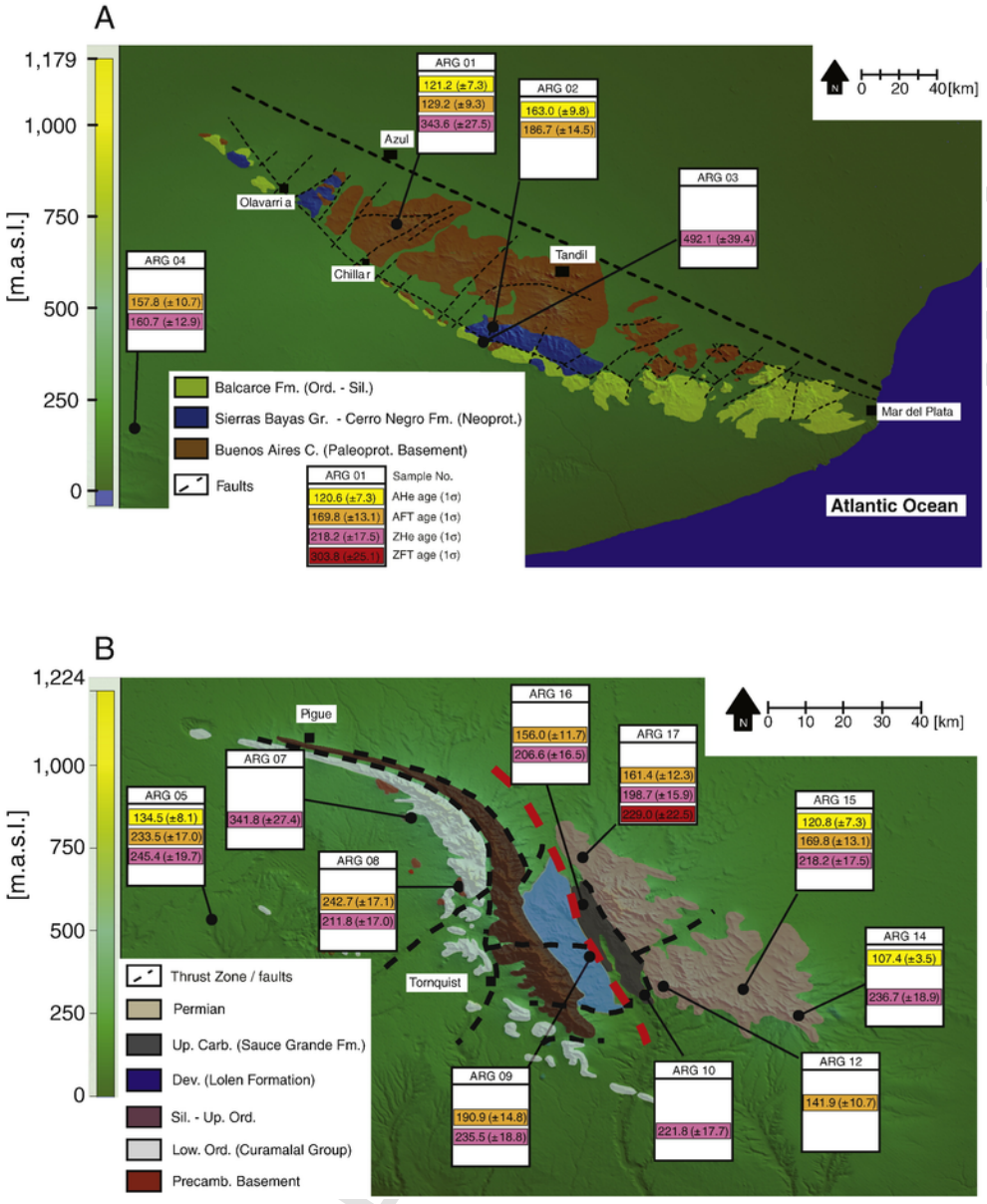

Fig. 3. A) Geological map of the Sierras Septentrionales combined with the DEM-90 m (redrawn after Cingolani, 2011) with regional distribution of thermochronological ages. B) Geological map of the Sierras Australes combined with the DEM-90 m (redrawn after Buggisch, 1987, Suero, 1972). The thrust zone is adapted from Cobbold et al., (1986), Rossello et al. (1997), and Tomezzoli (2001) with regional distribution of thermochronological ages.

1992; Lisker et al., 2009). The temperature sensitive annealing of fission-tracks in apatite is constraint by two important effects: 1.) The crystallographic orientation of the spontaneous tracks, and 2.) The chemical composition of apatite. Spontaneous tracks orthogonal to the c-axis anneal more rapid than tracks parallel to the c-axis (Green and Durrani, 1977; Green, 1981, 1988; Laslett et al., 1984; Donelick et al., 1999). Total annealing temperature of FT in apatite is governed by the fluorine- (90–110 °C/10 Myr) and chlorine content (110–150 °C/10 Myr). The partial annealing zone of FTs in apatite extend from total annealing temperature to 60 °C/10 Myr. The change of arithmetic mean fission-track etch pit size parallel to the crystallographic c-axis (kinetic parameter D_{par}) depends on the chemical composition and the etching conditions (5.5 N HNO_3, 20 s, 21 °C) (Sobel and Seward, 2010, and literature therein). In zircon, the annealing process is governed by the degree of metamictization. Metamictization is caused by the interaction of the alpha-recoil nucleus, and the fission fragments with the crystal lattice of zircon (Nasdala, 2009; Garver, 2002). The total annealing temperature of zircon decreases from 330 °C/10 Myr to 190 °C/10 Myr with increasing metamictization (Brix et al., 2002; Garver and Kamp, 2002; Rahn et al., 2004). With an average degree of metamictization temperatures of about 240 °C/10 Myr are assumed by Yamada et al. (1995), and Hurford (1986).

Apatite and zircon grains were concentrated by the standard techniques for heavy mineral separation (Grist and Ravenhurst, 1992a, 1992b; Donelick et al., 2005). After mounting apatite grains in Epofix, the polished mounts were etched in 5.5 N HNO_3 for 20 ± 1 s at 21 ± 1 °C, and thereafter covered by U-free detection muscovite. The covered apatite grain mounts, as well as two Durango apatite age standards and three glass neutron dosimeters (CN5, top, middle, and bottom of sample batch) were irradiated with thermal neutrons at the

Table 1
Summary of the dated samples with corresponding sample numbers, lithologies, stratigraphic ages and coordinates.

Sample number	Lithology	Stratigraphy	Formation	Latitude	Longitude	AltitudPlease change Altiude to Elevation.e above sea level [m]
Sierras Septentrionales						
ARG 01	Orthogneiss	Palaeoproterozoic	Buenos Aires Complex	37° 3.780′ S	59° 57.319′ W	153
ARG 02	Orthogneiss	Palaeoproterozoic	Buenos Aires Complex	37° 35.648′ S	59° 24.898′ W	273
ARG 03	Rhyolite	Ordovician	Ordovician	37° 38.529′ S	59° 25.541′ W	261
Claromecó basin						
ARG 04	Clay-/siltstone	Upper Permian	Tunas	38° 3.307′ S	60° 3.938′ W	139
Sierras Australes						
West of Sauce Grande wrench						
ARG 07	Ignimbrite	Upper Proterozoic		37° 46.446′ S	62° 17.345′ W	375
ARG 08	Paragneiss	Precambrian		37° 56.375′ S	62° 10.305′ W	426
ARG 09	Sandstone	Upper Devonian	Lolen	38° 3.958′ S	61° 52.247′ W	353
ARG 09 A	Granitic pebble of Diamictite	Upper Carboniferous	Sauce Grande	38° 3.958′ S	61° 52.247′ W	353
East of Sauce Grande wrench						
ARG 06	Granite	Carboniferous-Jurassic		38° 4.238′ S	62° 27.86′ W	212
ARG 10	Granitic pebble of Diamictite	Upper Carboniferous	Sauce Grande	38° 7.816′ S	61° 46.682′ W	269
ARG 11	Granitic pebble of Diamictite	Upper Carboniferous	Sauce Grande	38° 7.401′ S	61° 48.066′ W	258
ARG 12	Sandstone	Permian	Piedra Azul	38° 7.356′ S	61° 43.775′ W	319
ARG 13	Sandstone	Upper Permian	Tunas	38° 3.516′ S	61° 42.304′ W	315
ARG 14	Sandstone	Upper Permian	Tunas	38° 15.626′ S	61° 21.537′ W	367
ARG 15	Sandstone	Upper Permian	Tunas	38° 12.629′ S	61° 29.063′ W	399
ARG 16	Diamictite	Upper Carboniferous	Sauce Grande	38° 0.287′ S	61° 52.046′ W	381
ARG 17	Sandstone	Upper Permian	Tunas	37° 53.213′ S	61° 51.585′ W	416
Lopez Lecube intrusion						
ARG 05	Syenite	Permian	245 ± 12 Ma	38° 7.929′ S	62° 42.613′ W	96

research reactor FRM II, Munich. After irradiation, the detection micas were etched in 48% HF for 20 ± 1 min at 20 ± 1 °C.

Polished zircon grains Teflon mounts were etched in a NaOH – KOH eutectic melt at 228 ± 5 °C for 3–13 h. The zircon mounts were covered with a U-free detection mica, and also irradiated together with glass neutron dosimeter (CN1) and Fish River Canyon tuff zircon age standards by thermal neutrons in the research reactor FRM II in Munich, Germany. The corresponding external mica detectors were etched in 48% HF for 20 min at 20 ± 1 °C. Area densities (tracks/cm^2) of spontaneous and induced tracks, distribution of horizontal confined spontaneous fission-track length (length and c-axis related angle), and the c-axis oriented etch pit diameters (Dpar®, Donelick, 1993, 1995) were measured with the Heidelberg FT-1 system (Karl et al., 2013). The presented ages are central ages and were calculated by applying the ζ-method after Hurford and Green (1982, 1983). The ζ-values of 336.83 ± 19.51 a/cm^2 for CN5 (apatite) and 123.00 ± 6.08 a/cm^2 for CN1 (zircon) were gained using Durango apatite and Fish River Canyon zircon age standards. All ages, 1ζ-errors, and radial plots were calculated and drawn using the computer code `TRACKKEY`(Dunkl, 2002) and displayed as recommended by Hurford (1990) (Tables 2–4).

3.2. (U-Th-Sm)/He-dating

The (U-Th-Sm)/He thermochronology is based on the accumulation of ^{4}He during the α-disintegration of ^{238}U, ^{235}U, ^{232}Th, their daughter products and ^{147}Sm. In general, the Tc (Dodson, 1973) of the apatite He system is ~ 75 °C/1 Myr for cooling rates of 10 °C/Myr, subgrain domain sizes > 60 μm, an activation energy of about 36 kcal/mol, and a log(D_0) of 7.7 ± 0.6 cm^2/s (Farley, 2000). The crystal size itself represents the effective diffusion domain in apatites, with larger crystals having a higher closure temperature (Farley, 2000; Reiners and Farley, 2001). A correction has to be applied for the loss/gain of radiogenic He generated within an outer rim of the mineral grain by the α-stopping distances (apatite: 25 μm) (Wolf et al., 1996, Farley et al., 1996, Farley, 2002). While the α-ejection correction is applied more routinely, the recently introduced correction for radiation damage is still in progress (Shuster et al., 2006; Shuster and Farley, 2009; Flowers et al., 2007, 2009). Shuster et al. (2006)

Table 2
Summary of apatite (U-Th-Sm)/He data. M: mass, contributing U, Th, Sm, and He concentration, eU = [U] + 0.235 [Th] (concentration in μg/g), Ft: α ejection factor for apatite and zircon calculated after Farley et al. (1996), Raw (raw) ages and 1σ error for α-ejection with accordant 1σ error (Orthogn. = Orthogneiss).

S.-no.	Lithology	U [μg/g]	Th [μg/g]	Sm [μg/g]	eU [μg/g]	Th/U	He [nmol/g]	M (μg)	Ft	Raw age [Ma]	± 1σ [Ma]	Age [Ma]	± 1σ [Ma]
Sierras Septentrionales													
ARG 01-1	Othogn.	96.7	121.8	125.0	125.3	1.3	55.9	2.28	0.67	81.5	4.9	121.2	7.3
ARG 01-2	Othogn.	109.2	112.7	112.7	135.7	1.1	78.3	2.11	0.65	105.4	6.3	161.8	9.7
ARG 01-3	Othogn.	123.0	174.4	166.1	163.9	1.4	68.5	2.24	0.67	76.3	4.6	114.1	6.8
ARG 02-1	Othogn.	3.3	0.7	31.1	3.6	0.2	2.0	1.06	0.61	98.9	5.9	163.0	9.8
ARG 02-2	Othogn.	18.3	1.6	32.6	18.8	0.1	8.7	0.98	0.59	84.7	5.1	143.0	8.5
ARG 02-3	Othogn.	5.2	0.3	23.3	5.4	0.1	2.6	2.74	0.71	86.5	5.2	121.6	7.2
Sierras Australes													
West of Sauce Grande wrench													
ARG 05-1	Syenite	12.0	87.7	26.3	32.4	7.3	18.3	9.92	0.77	102.4	6.1	132.6	7.9
ARG 05-2	Syenite	21.0	67.0	87.3	36.9	3.2	14.6	3.15	0.69	71.6	4.3	103.3	6.2
ARG 05-3	Syenite	10.2	65.3	16.7	25.4	6.4	14.6	8.63	0.78	104.5	6.3	134.5	8.1
East of Sauce Grande wrench													
ARG 14-1	Sandstone	51.8	22.3	26.8	57.1	0.4	22.4	2.31	0.68	72.1	4.3	105.8	6.3
ARG 14-2	Sandstone	39.0	34.7	66.7	47.3	0.9	15.7	1.28	0.61	60.9	3.7	99.4	5.9
ARG 14-3	Sandstone	20.0	22.4	11.7	25.2	1.1	8.4	0.82	0.56	59.8	1.9	107.4	3.5
ARG 15-1	Sandstone	11.4	18.7	14.3	15.8	1.6	13.1	2.56	0.68	150.9	9.1	220.9	13.2
ARG 15-2	Sandstone	5.4	14.7	47.5	9.0	2.8	14.7	1.00	0.58	290.2	17.4	503.8	30.2
ARG 15-3	Sandstone	56.4	39.0	49.1	65.6	0.7	29.1	2.34	0.67	81.3	4.9	120.8	7.3

Table 3
Apatite fission-track data. U: uranium concentration in μg/g, n: number of counted grains, ρ_s: density of spontaneous tracks ($\times 10^5/cm^2$), N_s: number of spontaneous tracks, ρ_i: density of induced tracks ($\times 10^5/cm^2$), N_i: number of induced tracks, $P(\chi^2)$ is the probability that single grain ages are consistent and belong to the same population. Test is passed if $P(\chi^2) > 5\%$ (Galbraith, 1981). Ages calculated using a ζ-value of 336.83 (19.51) a/cm^2 for apatite, N_d = 15.148 tracks.

S.-no.	Elev. [m.a.s.l.]	Form. age	U ± std. [μg/g]	n	Sp. tracks		Ind. tracks		χ^2 [%]	Central age ± 1σ [Ma]
					ρ_s	N_s	ρ_i	N_i		
Sierras Septentrionales										
ARG 01	153	Palaeoproterozoic	38.5 ± 16.9	20	23.349	867	43.519	1616	54.13	129.2 ± 9.3
ARG 02	273	Palaeoproterozoic	14.8 ± 5.6	20	14.974	678	19.125	866	96.27	186.7 ± 14.5
Claromecó basin										
ARG 04	139	Tunas Fm. Up. Perm.	35.6 ± 14.6	20	25.684	1370	38.713	2065	100	157.8 ± 10.7
Sierras Australes										
West of Sauce Grande wrench										
ARG 08	426	Precambrian.	36.3 ± 24.3	20	39.174	1315	37.804	1269	99.88	242.7 ± 17.1
ARG 09	353	Lolen Fm. Up. Devon.	25.3 ± 15.2	20	22.071	1021	27.367	1266	15.25	190.9 ± 14.8
East of Sauce Grande wrench										
ARG 12	319	Piedra Azul Fm. Perm.	41.3 ± 17.3	20	26.872	714	44.260	1176	99.8	141.9 ± 10.7
ARG 15	399	Tunas Fm. Up. Perm.	26.4 ± 14.8	20	19.796	1084	27.430	1502	4.22	169.8 ± 13.1
ARG 16	381	Sauce Grande Fm.	18.6 ± 10.6	17	13.684	839	20.257	1242	35.11	156.0 ± 11.7
ARG 17	416	Tunas Fm. Up. Perm.	29.2 ± 15.2	20	22.433	869	32.088	1243	33.64	161.4 ± 12.3
Lopez Lecube intrusion										
ARG 05	96	Permian	26.6 ± 7.0	18	30.693	1056	30.655	1065	100	233.5 ± 17.0

noted that ^{4}He diffusion in apatite is impeded by radiation-induced damage to the crystal structure. Their ^{4}He production-diffusion model predicts that the effective ^{4}He closure temperature of apatite will vary with cooling rate and effective uranium concentration (eU), and may differ from the commonly assumed T_c of ~ 75 °C/1 Myr by up to ± 15 °C (Shuster et al., 2006, Shuster and Farley, 2009). To account for the accumulation of crystal defects due to the radioactive decay the eU factor (eU = [U] + 0.235 [Th]; concentrations in μg/g) was introduced (Shuster et al., 2006). Flowers et al. (2009) published a new kinetic model (RDAAM) that describes the annealing kinetics with respect to the effective fission-track density as a proxy for accumulated radiation damage. Basically, the new RDAAM is a variation of the older helium-trapping model (HeTM; Shuster et al., 2006), by taking the effective fission-track density instead of the He concentration into account.

For the zircon He system the closure temperature is ~ 180 °C/1 Myr, with the HePRZ in the range of ~ 170–200 °C/Ma, given a cooling rate of 10 °C/Myr, a crystal half width of 60 μm and an activation energy of ~ 170 kJ/mol (Reiners et al., 2002, 2004).

While radiation damage in apatite leads to increased cooling ages, He diffusivity in zircon is affected by radiation damage, resulting either in younger or older cooling ages than it would be the case for a sample not influenced by radiation damage (Reiners et al., 2004, Farley, 2007, Guenthner et al., 2013). The He diffusivity of a zircon can either be decreased, as He is trapped, resulting in a positive correlation with the eU content; or the He diffusivity can increase as numerous traps are connected, resulting in a negative correlation (cp.

Table 4
Apatite confined spontaneous fission-track length and Dpar data. n CT: number of measured confined spontaneous fission-tracks, CT mean: mean confined spontaneous fission-track length, std.: standard deviation, skew: skewness of distribution relative to the mean value (measure of asymmetry of the distribution), Lc mean: mean confined spontaneous fission-track length after c-axis correction, n Dpar: number of etch pit diameters measured, Dpar mean: mean etch pit diameter.

Sample number	n CT	CT mean [μm]	CT std. [μm]	CT skew	Lc mean [μm]	Lc std. [μm]	Lc skew	n Dpar	Dpar mean [μm]	Dpar std. [μm]	Dpar skew
Sierras Septentrionales											
ARG 01	51	11.7	2.1	− 0.304	13.2	1.4	− 0.297	50	1.9	0.1	− 0.899
ARG 02	51	12.5	1.6	− 0.074	13.9	1.0	0.257	50	1.8	0.2	− 0.184
Sierras Australes											
West of Sauce Grande wrench											
ARG 05	56	11.7	1.6	0.074	13.4	1.2	− 0.029	55	1.9	0.2	0.239
ARG 08	51	13.0	1.6	− 0.118	14.3	1.1	− 0.171	50	1.8	0.2	− 0.722
ARG 09	48	12.9	1.7	− 0.110	14.2	1.2	− 0.266	55	1.8	0.2	− 1.221
East of Sauce Grande wrench											
ARG 12	52	11.3	1.8	0.224	13.0	1.4	− 0.302	55	1.7	0.2	1.112
ARG 15	79	13.1	1.4	− 0.639	14.3	1.1	− 1.339	70	1.9	0.2	0.209

Guenthner et al., 2010). Such an inverse correlation can be visualized by plotting the ZHe-age as a function of eU.

The apatite and zircon single grain selection for (U-Th-Sm)/He dating was done in the Institute of Earth Sciences in Heidelberg by using an Olympus SZX 16 stereo microscope. Size measurements and shape description (photos) were taken by using the software Olympus Stream Enterprise v. 1.5.1. The aliquots were filled in Pt foil tubes and sent to the (U-Th-Sm)/He laboratory of Prof. Daniel F. Stockli at the Department of Geology of the University of Kansas. There the grains were loaded in the automated (U-Th-Sm)/He laser extraction line for extracting the radiogenic ^{4}He in an ultrahigh vacuum chamber through heating with an Nd-YAG laser. The released gas was measured and quantified in terms of $^{4}He/^{3}He$ ratios with a quadrupole He mass spectrometry system. After complete degassing the aliquots were unwrapped and dissolved for U, Th, and Sm determination. For apatite, samples were spiked with ^{235}U, ^{230}Th, and ^{149}Sm and dissolved in 30% HNO_3 (90 °C for 1 h) whereas zircons were dissolved using standard U-Pb double pressure-vessel digestion procedures (HF-HNO_3 and HCl) for 4 days. After dissolution, the single aliquots were analysed in consideration of U, Th, and Sm using a VG PlasmaQuad IIXS Inductively Coupled Plasma Mass Spectrometer (ICP-MS). Further information of the analytical method is documented on the homepage of the Department of Geology of the University of Kansas (www.geo.ku.edu/programs/tectonics). In order to minimize effects caused by undetected mineral inclusions, both mineral phases i.e. zircon and apatite were bombed to ensure complete digestions as described in Vermeesch et al. (2007). Reported errors are 6% for apatite and 8% for zircon based on the respective reproducibility of the Fish River Canyon age standards. If the reproducibility of aliquots within one sample is poorer than 6% or 8% respectively the corresponding error is reported. All quantities were measured on a single crystal to eliminate uncertainties that arise from grain to grain heterogeneities; resulting He ages were corrected for α-ejection (Tables 5 and 6). For further details on the He analytical techniques see Farley (2002), Mitchell and Reiners (2003), and Reiners (2005). (See Table 7.)

3.3. Numerical modelling of thermal history

One aim of thermochronological analysis is to determine the cooling and exhumation rates for crustal segments. Beside direct quantification by using age-elevation plots, exhumation rates can be calculated by combining the cooling history determined by numerical modelling with assumed past geothermal gradients. The software code HeFTy (Ketcham, 2005; Ketcham et al., 2007a, 2007b, 2009), allows testing various geological time-temperature (t-T) evolutions (heating and cooling histories) against the thermochronological data set. Representative geological time-temperature histories are constructed from published geological data. For example: as Zambrano and Urien (1970) report Lower Cretaceous volcanic units in the Salado basin, we set up two different possible thermal histories (one with a Cretaceous reheating-event and one without a reheating-event) for the samples (#ARG 01, #ARG 02, #ARG 03) from the Sierras Septentrionales. Additionally, the models were forced to be near surface conditions during Cambrian, as in both mountain ranges the Cambrian is missing. #ARG 05 (Permian syenite intrusion) was modelled with an initial temperature condition up to 500 °C, due to published U-Pb and K/Ar data with ages of about 250 Ma.

The thermochronological data sets used for the modelling are:

- AFT: single grain ages, confined spontaneous fission-track length distribution (> 50 individual length) corrected for c-axis related angle (Donelick et al., 1999; Ketcham, 2009), etch pit size (Dpar®), annealing kinetics of Ketcham et al. (2007a, 2007b):

– ZFT: only the central age
– AHe: U-, Th-, and Sm-concentration, radius of the single grains, uncorrected single grain ages, diffusion kinetics of Flowers et al. (2009).
– ZHe: U-, Th-, and Sm-concentration, radius of the single grains, uncorrected single grain ages, diffusion kinetics of Reiners et al. (2004).

The software code allows creating t-T forward models for the AFT models by calculating the apatite fission-track length distribution, and the apparent age and AHe and ZHe models by calculating a model age and a He-distribution within the grains. The initial inverse modelling is based on the best forward model revealed. The geologically framed t-T coordinates are included in the computer code as t-T windows, which cover the possible error range of the t-T coordinates. For each sample, we performed the numerical modelling as long as the program provides the same t-T evolution after the runs. In all cases presented in this publication, we tested 50.000 single t-T paths against the thermochronological data set. Statistical tests are used to compare the calculated age and confined spontaneous fission-track length distribution against the determined thermochronological data set. The statistical test calculates a "goodness of fit" (GOF) value between 0 and 1. GOF values of ≥ 0.05 (≥ 5%) are an "acceptable" result (displayed as greens paths), GOF values ≥ 0.5 (≥ 50%) are a "good" result (displayed as purple paths). Furthermore, the program displays the t-T path with the "best GOF" fitting (Ketcham, 2009;

Table 5
Summary of zircon (U-Th)/He data. M: mass, contributing U, Th, Sm, and He concentration, eU = [U] + 0.235 [Th] (concentration in μg/g), Ft: α-ejection factor for apatite and zircon calculated after Farley et al. (1996), Raw (raw) ages and 1σ error for α-ejection with accordant 1σ error. (Orthogn. = Orthogneiss, Sandst. = Sandstone, Ignimbr. = Ignimbrite).

S.-no.	Lithology	U [μg/g]	Th [μg/g]	Sm [μg/g]	eU [μg/g]	Th/U	He [nmol/g]	M (μg)	Ft	Raw age [Ma]	± 1σ [Ma]	Age [Ma]	± 1σ [Ma]
Sierras Septentrionales													
zARG 01-1	Othogn.	130.3	70.3	2.3	146.5	0.54	187.1	2.29	0.67	231.6	18.5	343.6	27.5
zARG 01-2	Othogn.	137.9	50.5	2.3	149.5	0.37	306.6	2.52	0.67	366.7	29.3	547.0	43.7
zARG 01-3	Othogn.	193.8	60.6	4.6	207.7	0.31	211.4	5.33	0.75	185.4	14.8	247.6	19.8
zARG 03-1	Rhyolite	249.7	146.5	19.6	283.5	0.59	316.1	8.27	0.76	202.5	16.2	264.9	21.2
zARG 03-2	Rhyolite	64.1	59.0	1.2	77.7	0.92	154.6	4.70	0.72	355.9	28.5	492.1	39.4
zARG 03-3	Rhyolite	114.1	106.6	5.3	138.7	0.93	240.0	4.77	0.73	310.9	24.9	428.7	34.2
Claromecó basin													
zARG 04-1	Sandst.	465.7	192.9	27.0	510.2	0.41	410.4	6.52	0.76	147.0	11.8	192.6	15.4
zARG 04-2	Sandst.	493.9	242.5	5.8	549.7	0.49	395.2	5.35	0.74	131.6	10.5	176.6	14.1
zARG 04-3	Sandst.	186.3	121.9	2.3	214.4	0.65	133.1	3.31	0.71	113.7	9.1	160.7	12.9
Sierras Australes													
West of Sauce Grande wrench													
zARG 05-1	Syenite	263.6	220.5	1.0	314.4	0.84	363.5	8.70	0.78	209.8	16.8	270.3	21.6
zARG 05-2	Syenite	200.0	205.6	3.1	247.3	1.03	271.1	11.20	0.79	199.0	15.9	251.9	20.1
zARG 05-3	Syenite	336.2	300.7	4.2	405.5	0.89	447.9	6.08	0.75	200.6	16.0	267.4	21.3
zARG 05-1-1	Syenite	200.2	192.9	1.4	244.6	0.96	255.7	8.85	0.77	190.0	15.2	246.4	19.7
zARG 05-1-2	Syenite	289.5	254.8	4.7	348.1	0.88	365.1	9.11	0.76	190.6	15.2	250.3	20.0
zARG 05-1-3	Syenite	289.1	277.4	4.7	353.0	0.96	319.2	5.47	0.73	164.7	13.2	224.1	17.9
zARG 07-2	Ignimbr.	221.1	173.6	5.7	261.1	0.79	319.6	2.03	0.65	221.9	17.8	341.8	27.4
zARG 07-3	Ignimbr.	285.1	212.2	4.7	334.0	0.74	307.0	1.71	0.62	167.4	13.4	269.2	21.5
zARG 08-1	Paragneis	407.4	86.8	1.5	427.4	0.21	421.2	10.17	0.80	179.7	14.4	225.8	18.1
zARG 08-2	Paragneis	258.4	64.3	1.3	273.3	0.25	252.3	9.77	0.80	168.5	13.5	211.8	17.0
zARG 08-3	Paragneis	321.5	55.6	1.9	334.3	0.17	267.0	3.70	0.72	146.1	11.7	203.6	16.3
zARG 09-1	Sandst.	195.0	167.4	7.0	233.6	0.86	521.5	8.57	0.78	397.9	31.8	512.8	41.0
zARG 09-2	Sandst.	227.7	104.9	5.7	251.8	0.46	255.4	8.69	0.78	184.6	14.8	235.5	18.8
zARG 09-3	Sandst.	111.8	67.8	3.5	127.4	0.61	320.7	6.52	0.76	446.1	35.7	584.6	46.8
East of Sauce Grande wrench													
zARG 10-1	Pebble Diamictite	399.4	615.3	7.6	541.1	1.54	493.4	6.41	0.75	165.8	13.3	221.8	17.7
zARG 10-3	Pebble Diamictite	1037.4	1268.7	39.9	1329.7	1.22	874.9	5.34	0.74	120.2	9.6	161.7	12.9
zARG 14-1	Sandst.	415.9	123.1	12.4	444.3	0.30	351.8	10.64	0.80	144.8	11.6	181.1	14.5
zARG 14-2	Sandst.	485.2	152.0	1.9	520.2	0.31	446.7	5.20	0.74	156.9	12.5	212.2	17.0
zARG 14-3	Sandst.	207.7	82.1	1.0	226.6	0.40	231.5	9.63	0.79	186.0	14.9	236.7	18.9
zARG 15-1	Sandst.	346.7	109.0	2.1	371.8	0.31	310.2	3.90	0.72	152.5	12.2	211.4	16.91
zARG 15-2	Sandst.	175.6	148.9	0.8	209.9	0.85	177.5	5.36	0.74	154.2	12.3	207.1	16.57
zARG 15-3	Sandst.	60.8	45.0	1.4	71.1	0.74	62.9	4.82	0.74	161.2	12.9	218.2	17.45
zARG 16-1	Diamictite	161.7	170.8	2.8	201.0	1.06	148.7	2.62	0.66	135.0	10.8	204.7	16.38
zARG 16-2	Diamictite	69.2	56.5	1.2	82.2	0.82	64.8	3.97	0.70	143.8	11.5	206.6	16.53
zARG 16-3	Diamictite	388.8	214.8	5.5	438.2	0.55	402.5	4.98	0.74	167.5	13.4	226.9	18.16
zARG 17-1	Sandst.	137.0	51.6	1.2	148.8	0.38	126.7	8.37	0.78	155.4	12.4	198.7	15.90
zARG 17-2	Sandst.	231.5	75.5	1.5	248.9	0.33	228.0	8.66	0.79	167.2	13.4	212.5	17.00
zARG 17-3	Sandst.	230.4	75.8	0.8	247.9	0.33	231.8	6.77	0.77	170.6	13.6	221.4	17.71

Ketcham et al., 2009). This path must neither be the right nor the only temperature history.

4. Thermochronological data and t-T modelling

All thermochronological ages are younger than the corresponding sedimentation, intrusion or metamorphic ages (Figs. 9Please cahnge Fig. 9 to Figs. 3A, 3B. And Tables 2-6. and 10; Tables **2**–**5**). Single grain apatite (U-Th-Sm)/He-ages of 5 samples range between 99.4 ± 5.9 Ma (#ARG 14-2) and 503.8 ± 30.2 Ma (#ARG 15-2). Most of the single grain ages of one sample are similar in age. For the thermochronological interpretation (e.g. t-T path modelling) we chose those single grain ages that are represented by the lowest eU-value (Table **2**) meaning an age distribution between 107.4 ± 3.5 (#ARG 14-3) and 163.0 ± 9.8 Ma (#ARG 02-1).

Apatite fission-track ages of 10 samples vary between 129.2 ± 9.3 Ma (#ARG 01) and 242.7 ± 17.1 Ma (#ARG 08, Table **3**). The oldest and youngest AFT-ages are revealed from Precambrian metamorphic rocks. Most of the other AFT-ages are of Jurassic to Lower Cretaceous age. The confined spontaneous fission-track length distribution (CT) of 7 samples indicates a large variability with a mean length between 11.3 ± 1.8 μm (#ARG 12) and 13.1 ± 1.4 μm (#ARG 15, Table **4**). The sample quality allowed measuring between 48 and 79 individually confined spontaneous fission tracks in each sample. No bimodal distribution was detected. Applying the angle between the crystallographic orientation of the fission tracks and the c-axes of the apatite grain lead to a much narrower c-axes corrected confined spontaneous fission-track length distribution (Lc) of 13.0 ± 1.4 μm (#ARG 12) and 14.3 ± 1.1 μm (#ARG 15). The length of the etch pits (Dpar) of all samples are within error the same with an average value of 1.8 ± 0.2 μm indicating fluorine-rich apatites (Donelick et al., 2005; Carlson et al., 1999).

Single grain zircon (U-Th-Sm)/He-ages of 12 samples range between 160.7 ± 12.9 Ma (#ARG 04-3) and 584.6 ± 46.8 Myr (#ARG 09-3, Table **5**). Most of the single grain ages of each sample are very narrow in age. The zircon grains we analysed display a positive e-functional correlation between the eU-value and the determined age (Fig. 4). Such a correlation is often seen in such data. Applying the eU-value as a selection criterion we chose zircon grains that are characterized by the lowest eU-value. The zircon grains show wide

Table 7
Separated t-T paths with exhumation rates of the research area. Exhumation rates were calculated including cooling rates and geothermal gradients. A geothermal gradient (Geother. Gradient) of 30 °C/km was used (Zeil, 1980). See text for further description.

Sample number	Elevation [m a.s.l.]	Cooling	t-t segment [Ma]	T-T segment [°C]	Cooling gradient [°C/Ma]	Geother. gradient [°C/km]	Exhumation rate [mm/a]	Δ t	Δ T
Sierras Septentrionales									
ARG 01-A	153	Cooling	370–320	230–60	3.40	30	0.113	50	170
ARG 01-A	153	Heating	320–260	60–95	0.58	30	− 0.019	60	35
ARG 01-A	153	Cooling	260–150	95–85	0.09	30	0.003	110	10
ARG 01-A	153	Cooling	150–0	85–20	0.57	30	0.014	150	65
ARG 01-B	153	Cooling	370–320	230–60	3.40	30	0.113	50	170
ARG 01-B	153	Heating	320–260	60–95	0.58	30	− 0.019	60	35
ARG 01-B	153	Cooling	260–210	95–50	0.90	30	0.030	50	45
ARG 01-B	153	Heating	210–150	50–95	1.00	30	− 0.033	45	45
ARG 01-B	153	Cooling	150–0	95–20	0.50	30	0.017	150	75
ARG 02-A	273	Heating	480–250	30–110	0.35	30	− 0.012	230	80
ARG 02-A	273	Cooling	250–130	110–40	0.58	30	0.019	120	70
ARG 02-A	273	Cooling	130–0	40–20	0.31	30	0.005	130	20
ARG 02-B	273	Heating	500–250	20–110	0.36	30	− 0.012	250	90
ARG 02-B	273	Cooling	250–190	110–60	0.83	30	0.028	60	50
ARG 02-B	273	Heating	190–160	60–70	0.33	30	− 0.011	30	10
ARG 02-B	273	Cooling	160–130	70–45	0.83	30	0.028	30	25
ARG 02-B	273	Cooling	130–0	45–20	0.19	30	0.006	130	25
Sierras Australes									
East of the Sauce Grande wrench									
ARG 12	319	Heating	280–250	20–240	7.33	30	− 0.244	30	220
ARG 12	319	Cooling	250–130	240–70	1.38	30	0.047	120	170
ARG 12	319	Nearly stable t-T-conditions	130–50	70–65	1.17	30	0.002	80	5
ARG 12	319	Cooling	50–0	40–65	0.20	30	0.017	50	25
ARG 14	367	Heating	250–220	20–185	5.50	30	− 0.183	30	165
ARG 14	367	Cooling	220–0	185–20	0.75	30	0.025	220	165
ARG 15	399	Heating	270–220	20–190	3.40	30	− 0.113	50	170
ARG 15	399	Cooling	220–185	190–70	3.43	30	0.114	35	120
ARG 15	399	Cooling	185–125	70–40	0.50	30	0.017	60	30
ARG 15	399	Cooling	125–0	40–20	0.16	30	0.005	125	20
ARG 16	381	Heating	320–200	20–185	1.38	30	− 0.046	120	165
ARG 16	381	Stable t-T-conditions	200–160	185–184	0.03	30	0.001	40	1
ARG 16	381	Cooling	160–155	184–85	4.95	30	0.008	20	5
ARG 16	381	Cooling	155–0	85–20	0.46	30	0.037	140	155
ARG 17	416	Heating	280–250	20–100	2.33	30	− 0.078	30	80
ARG 17	416	Heating	250–215	100–210	3.14	30	− 0.105	35	110
ARG 17	416	Cooling	215–155	210–90	2.00	30	0.067	60	120
ARG 17	416	Cooling	155–0	90–20	0.58	30	0.015	155	70
West of the Sauce Grande wrench									
ARG 07	375	Cooling	340–280	190–110	0.50	30	0.017	160	80
ARG 07	375	Cooling	280–0	110–20	0.32	30	0.011	280	90
ARG 08	426	Heating	480–250	25–190	0.72	30	− 0.024	230	165
ARG 08	426	Cooling	250–225	190–60	5.2	30	0.173	25	130
ARG 08	426	Cooling	225–150	60–50	0.13	30	0.004	75	10
ARG 08	426	Cooling	150–100	50–25	0.5	30	0.017	50	25
ARG 08	426	Cooling	100–0	25–20	0.05	30	0.002	100	5
ARG 09	353	Heating	400–240	20–180	1.00	30	− 0.033	160	160
ARG 09	353	Cooling	240–200	180–65	2.88	30	0.096	40	115
ARG 09	353	Cooling	200–135	65–55	0.15	30	0.005	65	10
ARG 09	353	Cooling	135–95	55–25	0.75	30	0.025	40	30
ARG 09	353	Cooling	95–0	25–20	0.05	30	0.002	95	5
Lopez Lecube intrusion									
ARG 05	96	Cooling	260–250	370–75	29.50	30	0.983	10	295
ARG 05	96	Cooling	250–130	75–60	0.13	30	0.004	120	15
ARG 05	96	Cooling	130–0	60–20	0.46	30	0.015	130	40

spread in ZHe single grain age distribution between 160.7 ± 12.9 Ma (#ARG 04-3) and 492.1 ± 39.4 Ma (#ARG 03-2) (Fig. 5).

One zircon fission-track age could be measured so far. The ZFT-age of 229.0 ± 22.5 Ma (# ARG 17) is younger than the formation age of Upper Permian (Tunas Fm.) indicating that the sample has been heated above at least 190 °C for > 10 Ma after deposition (Table **6**). The ZHe-age (198.7 ± 15.90 Ma) of the same sample is within error the same. Both ages indicate exhumation in Lower Jurassic at about 200 Ma.

Within the Sierras Australes the large variation of AFT-ages at a narrow elevation range (Figs. 12–14)Please change (Figs. 12-14) to (Figs. 5A, 5B, 5C) might be related to the occurrence of the Sauce Grande wrench (SGW). East of the wrench area the AFT-ages vary around 160 Ma and west of around 240 Ma.

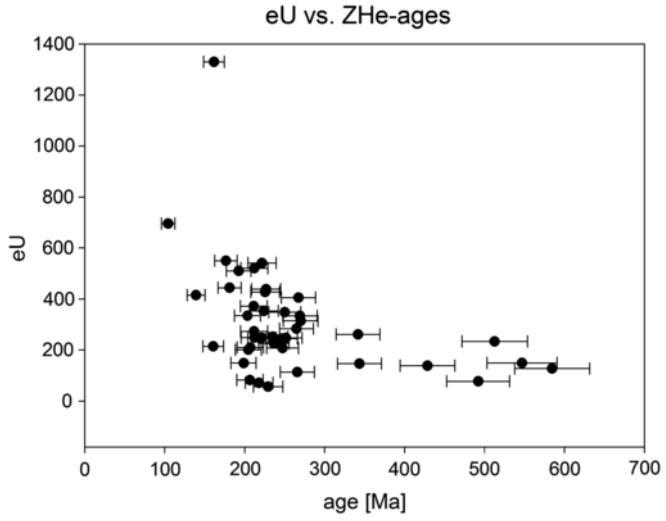

Fig. 4. Variation of single grain zircon (U-Th)/He ages with the related eU-value.

In the following subchapters, the thermochronological dataset is presented and sorted by the geographical distribution: Sierras Septentrionales, the Sierras Australes (east of the SGW) and the Claromecó basin, the Sierras Australes (west of the SGW), and the Permian intrusion of Lopez Lecube. All t-T models generated by testing published geological evolutionary scenarios against the thermochronological data set revealed acceptable, good, and best fit t-T paths. The interpretation used a calculated weighted mean t-T path that uses all acceptable and good t-T paths.

4.1. Sierra Septentrionales

The Sierra Septentrionales is bound by two major NW-SE trending fault systems and segmented by a large number of NE-SW-trending normal faults. The three samples were taken from different blocks separated by the NE-SW trending normal faults. All three samples are taken from elevations between 153 m a.s.l. and 273 m a.s.l. Two (#ARG01, #ARG02) of the three samples revealed enough apatite and zircon for multiple thermochronological dating(Figs. 5A, 5B, 5C). Despite the low difference in elevation the AHe-ages (121.2 ± 7.3 Ma versus 163.0 ± 9.8 Ma), the AFT-ages (129.2 ± 9.3 Ma versus 186.7 ± 14.5 Ma), and the ZHe-ages (343.6 ± 27.5 Ma versus 492.1 ± 39.4 Ma) vary significantly and, therefore, indicating movement along the normal faults during the Lower Cretaceous (Figs. 12–14).Please take (Figs. 12 - 14) out. Thank you. The C-axes corrected confined fission-track length distribution and the Dpar-values of both apatite-bearing samples are within error similar (13.2 ± 1.4 μm, 13.9 ± 1.0 μm) and around 1.8 ± 0.2 μm, respectively.

Testing the published geological evolution against the thermochronological data set leads to distinct t-T-histories (Figs. 6A, B and 7A, B). As Zambrano and Urien (1970) report Lower Cretaceous volcanic units in the neighbouring Salado basin, we set up two different possible geological evolutionary models. One geological evolutionary model assuming no volcanic activity (no reheating) at about 135 Ma (Figs. 6A and 7A) and one that assumed a volcanic activity (reheating) at about 135 Ma (Figs. 6B and 7B).

The t-T path for the "no reheating"-model of ARG 01 starts with a fast cooling (< 200 °C) at around 370 Ma. After reaching about 60 °C at about 320 Ma the temperature history is inverted to a phase of burial that reaches temperatures up to 95 °C at 260 Ma. Thereafter, slower cooling reaches 85 °C at 150 Ma and even slower cooling surface temperature in Quaternary. The second t-T model assuming a reheating by volcanic/magmatic activity revealed a temperature increase of 45 °C between 210 Ma (50 °C) and 150 Ma (95 °C). Thereafter, constant cooling reached surface temperature at recent time. The determined thermochronological data can be described by both geological assumptions. Therefore, the data so far cannot distinguish between a reheating or non-reheating in Lower Cretaceous time. Nev-

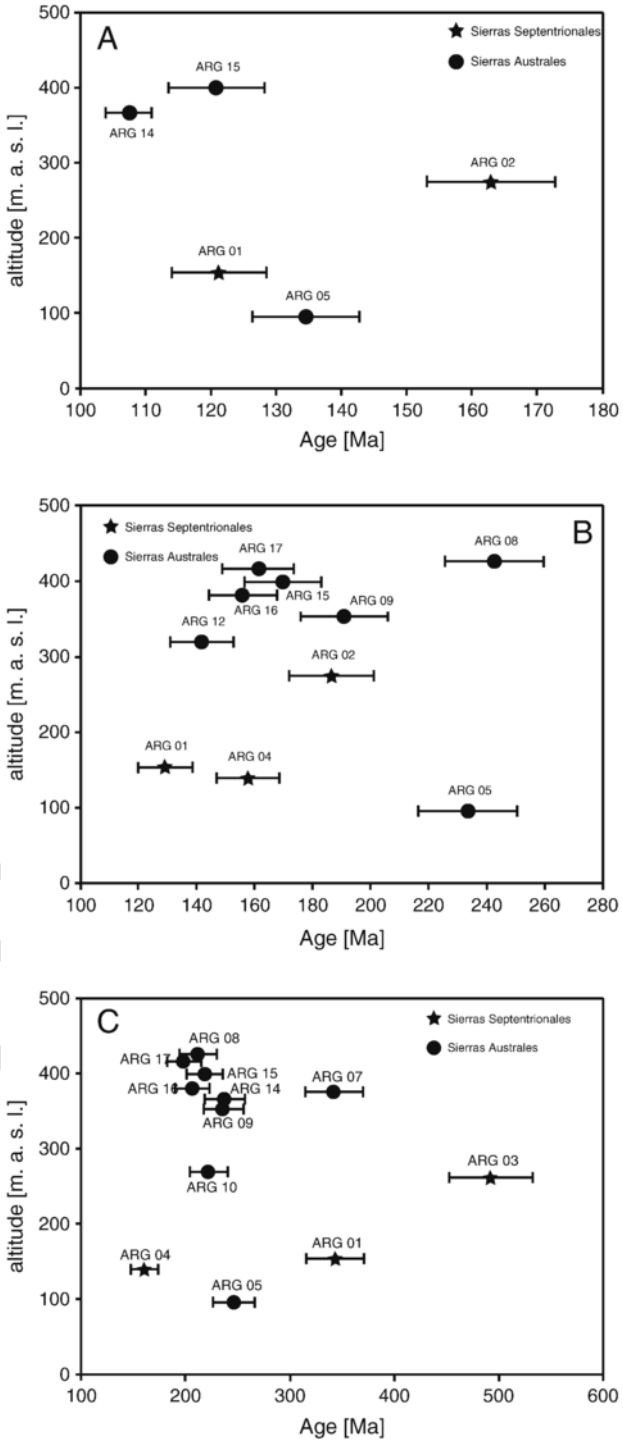

Fig. 5. A) Age-elevation plot of the AHe-data. B) Age-elevation plot of the AFT-data. C) Age-elevation plot of the ZHe-data.

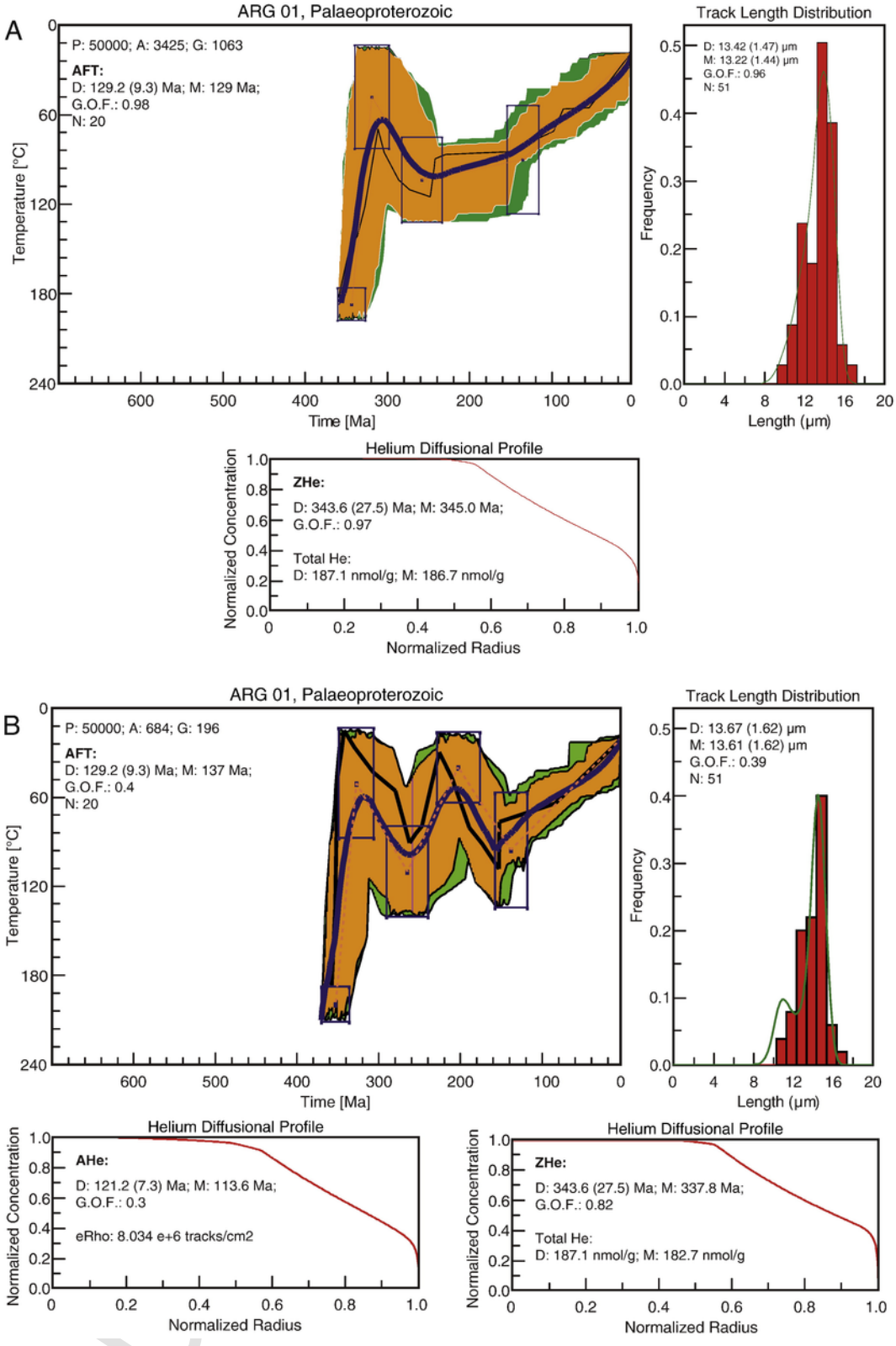

Fig. 6. t-T evolution of the sample #ARG 01 (Serra Septentrionales) with corresponding length-distribution and He-diffusional profile. A) without reheating. B) with reheating.

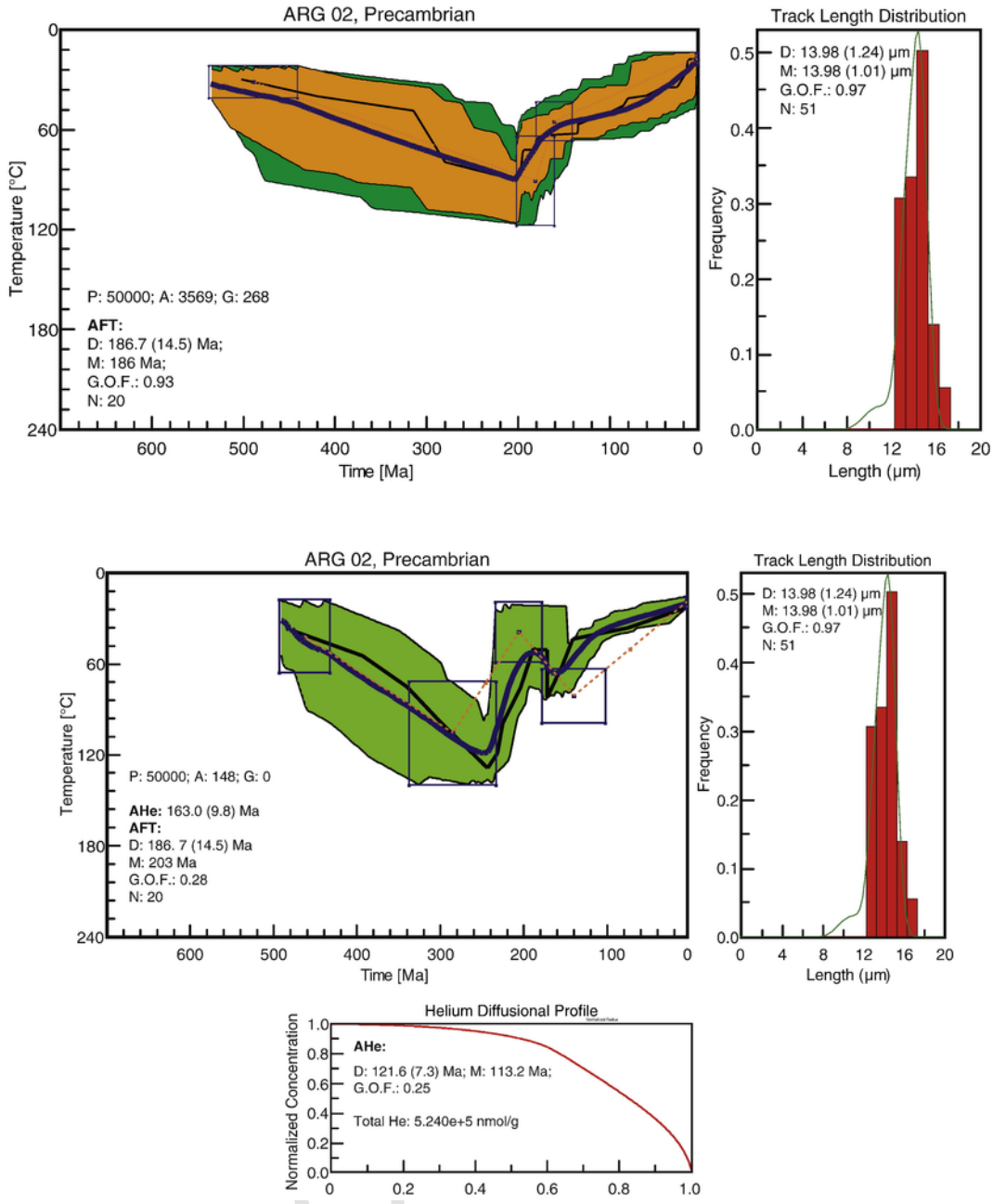

Fig. 7. t-T evolution of the sample #ARG 02 (Serra Septentrionales) with corresponding length-distribution. A) without reheating. B) with reheating.

ertheless, the AFT-age and the t-T history indicate an increase in cooling rate in Lower Cretaceous time.

As we do not have LTT-data of zircon for ARG 02 we started the initial t-T constrain at about 480 Ma simulating the first Palaeozoic sedimentation in Ordovician time. A phase of moderate heating from about 480 Ma until about 250 Ma is followed by a constant cooling, with only a lightly decrease of the cooling rate at about 130 Ma. The alternative model shows a second reheating starting at about 190 Ma and reaches 70 °C at about 160 Ma. Thereafter, a constant cooling reached surface temperature conditions in recent time. The third sample ARG 03 taken from the Precambrian units of the Sierras Septentrionales revealed a ZHe-age of 492.1 ± 39.4 Ma indicating that this area has been at a temperature of above 180 °C for > 1 Myr prior to the Early Ordovician.

4.2. Sierras Australes (east of the Sauce Grande wrench fault) and the Claromecó basin

One sample (#ARG 04, 139 m a.s.l) of the Permian Tunas formation has been taken from the Claromecó basin. The ZHe-age (160.7 ± 12.9 Ma) and AFT-age (157.8 ± 10.7 Ma) are within error the same thermochronological age indicating a fast cooling from about 180 °C to about 110 °C. Considering a thermal gradient of 30 °C and an annual surface temperature of about 15 °C > 2000 m of rocks was eroded during the Upper Jurassic to Lower Cretaceous.Pleaye leave > 2,000 m

Similarly, the samples #ARG 12, #ARG 15 - #ARG 17 from the Sierras Australes, east of the Sauce Grande wrench fault (SGW), are

characterized by AFT-ages of about 155 Ma. The ZHe-ages of the samples #ARG 10, #ARG 14 - #ARG 17 are significantly older and range from 236.7 ± 18.9 Ma to 198.7 ± 15.9 Ma. These ZHe-ages indicate a cooling below 180 °C/1 Ma during the Triassic and Jurassic. One ZFT-age (#ARG 17) indicate cooling below 240 °C/10 Ma during the Upper Triassic. The above-described data indicate a very distinct erosional history from Upper Triassic to Upper Jurassic for the eastern part of the Sierras Australes. As we do not know the Jurassic overburden of the recent rock surface in the Claromecó basin and the transport direction of the eroded material from the eastern part of the Sierras Australes it seems probable/possible that the eroded material was deposited in the Claromecó basin until the Upper Jurassic – Lower Cretaceous, and, thereafter, rapidly eroded again.

Apatite (U-Th-Sm)/He-ages of two samples from the Permian Tunas Formation range from 120.8 ± 7.3 Ma (#ARG 15) to 107.4 ± 3.5 Ma (#ARG 14) and, therefore, indicate the cooling below about 70 °C/1 Ma during the Cretaceous.

As the geological constrains of the Mesozoic and Cenozoic evolution of the Sierras Australes, east of the SGW, are very minor the t-T modelling used possible geological constrains in a broad manner. From Early Permian to Upper Triassic all numeric t-T models (Figs. 8A–C and 9A–C) of the samples from the Upper Carboniferous to Permian Sauce Grande Formation (#ARG 10, #ARG 16), the Per-

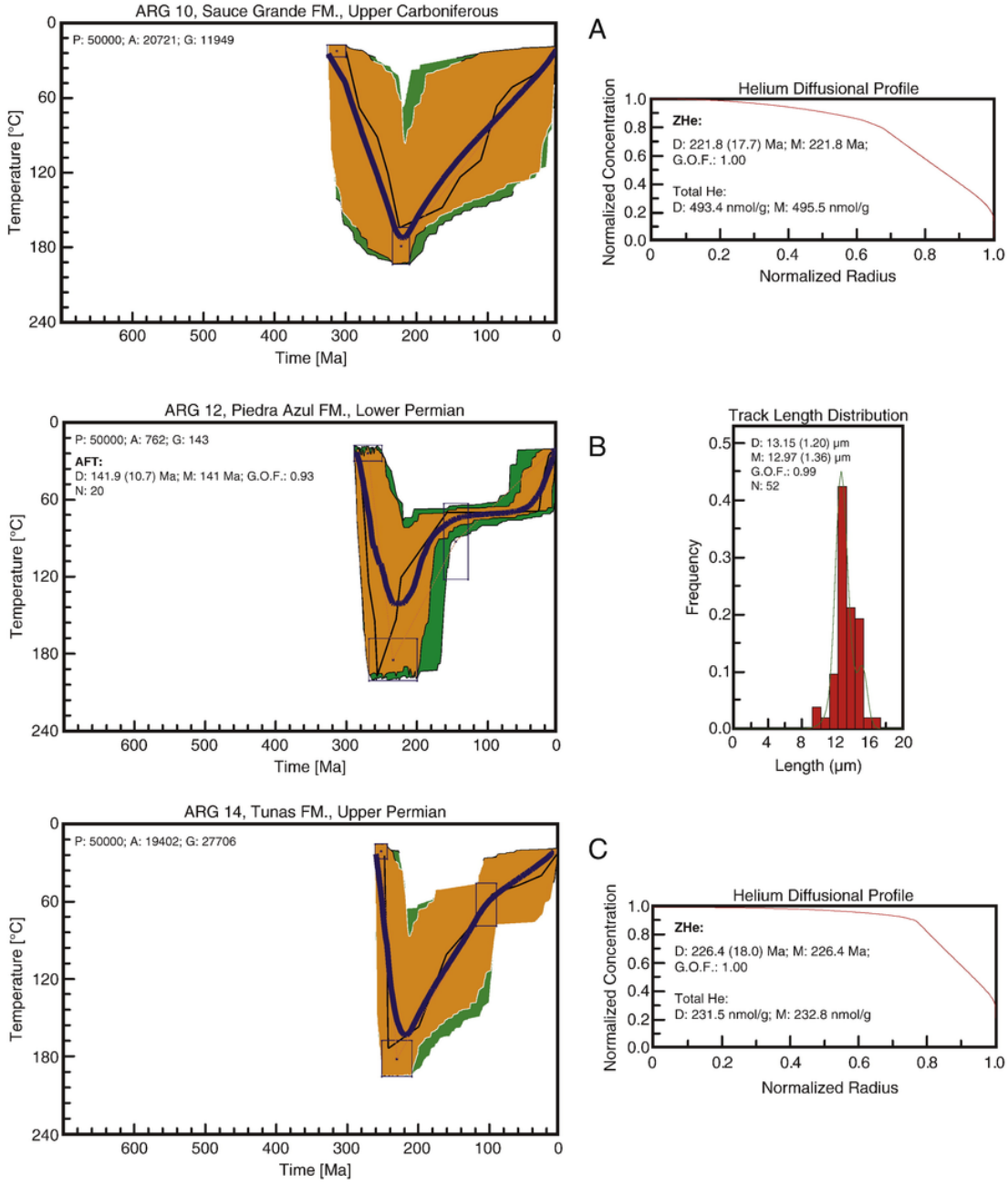

Fig. 8. A) t-T evolution of ARG 10 with corresponding length-distribution and He-diffusional profile. B) t-T evolution of ARG 12 with corresponding He-diffusional profile. C) t-T evolution of ARG 14 with corresponding length-distribution.

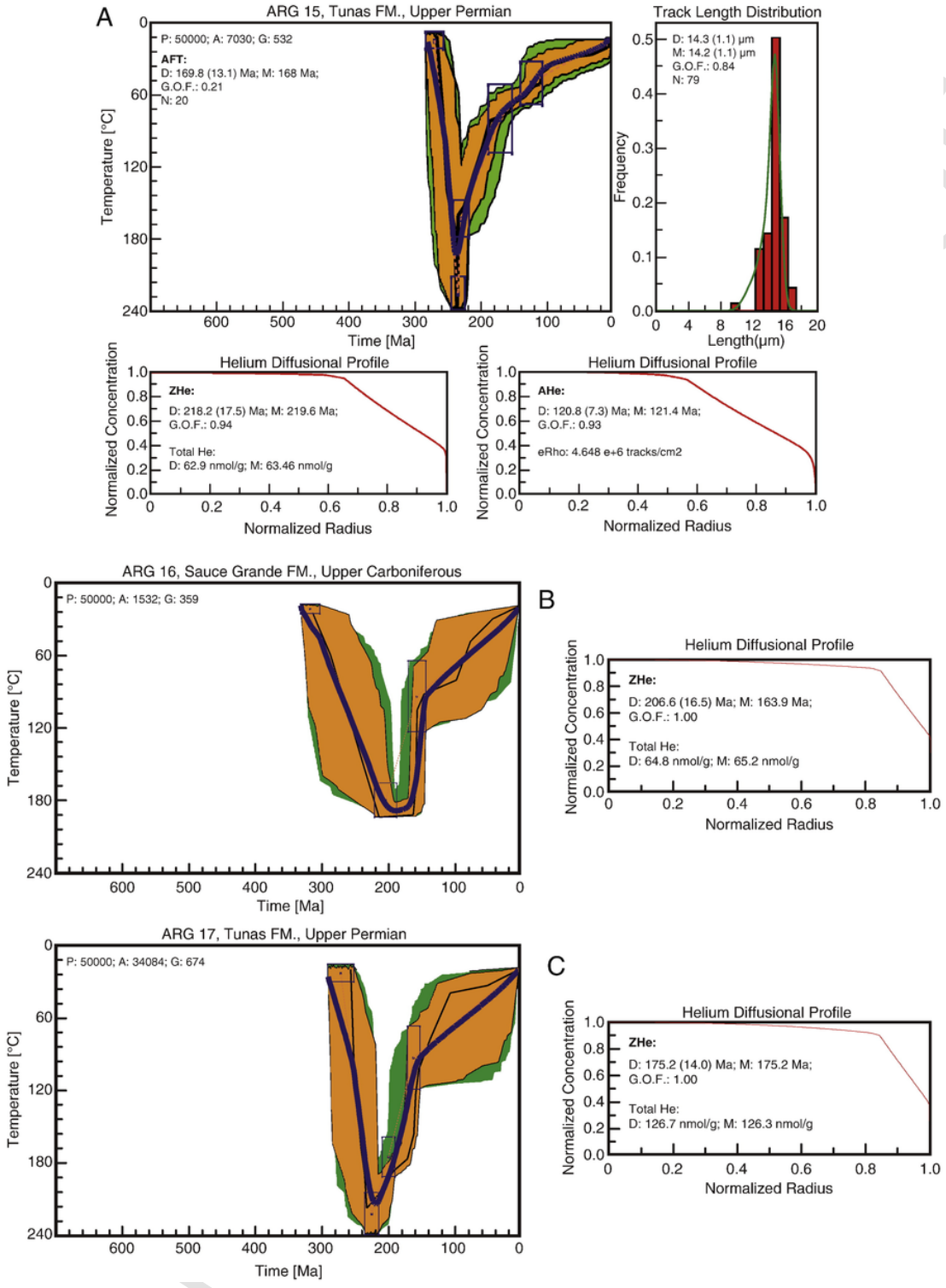

Fig. 9. A) t-T evolution of ARG 15 with corresponding length-distribution and He-diffusional profile. B) t-T evolution of ARG 16 with corresponding He-diffusional profile. C) t-T evolution of ARG 17 with corresponding length-distribution.

mian Piedra Azul Formation (#ARG 12), and the Permian Tunas Formation (#ARG 13 – #ARG 15, #ARG 17) indicate a fast temperature increase of about 165 °C from surface temperature to about 180 °C at about 220 Ma. If a surface temperature of 15 °C and a geothermal gradient of 30 °C/km is assumed, the surface rocks of today were overlain by up to 5 km of sedimentary rocks in the Upper Triassic. In all models the subsidence inverted and cooling started in the Upper Triassic. Sample #ARG 10 and #ARG 14 cooled constantly until ambient temperature was reached during the Quaternary. Sample #ARG 16 and #ARG 17 cooled rapidly until 155 Ma reaching a temperature of about 90 °C and, thereafter, cooled slower to ambient temperature in Quaternary. The Permian sandstone of the Tunas formation (#ARG

15) with three thermochronological ages (AHe, AFT, ZHe) cooled in three distinct steps from about 180 °C at 220 Ma to 70 °C at 185 Ma, from 70 °C to 40 °C at about 125 Ma, and, thereafter to surface temperature in Quaternary. The sandstone of the Permian Piedra Azul (#ARG 12) cooled to 70 °C at 130 Ma and kept at a similar temperature up to 50 Ma. A rapid cooling reached surface temperature in Quaternary.

4.3. Sierras Australes (west of the Sauce Grande wrench fault)

The Upper Proterozoic ignimbrite (#ARG 07) revealed the oldest zircon (U-Th)/He age of 341.8 ± 27.4 Ma indicating a cooling below about 180 °C during the Upper Carboniferous. As the second zircon grain with higher eU-value is much younger (269.2 ± 21.5 Ma) the transfer into geological interpretation is very weak. More zircon grains would have to be analysed. The ZHe age of the two other samples (#ARG 08 - Precambrian paragneiss; #ARG 09 - Upper Devonian sandstone) that were taken farther away from #ARG 07 are younger but within error both samples show the same age and indicate a Middle to Upper Triassic cooling age (211.8 ± 17.0 Ma; 235.5 ± 18.8 Ma, respectively). Two more zircon grains of #ARG 08 reveal within error the same Upper Triassic age of about 215 Ma (in average). In comparison to the samples from the eastern side of the SGW, the ZHe-ages are within error similar. Neoproterozoic ZHe-ages (512.8 ± 41.0 Ma; 584.6 ± 46.8 Ma) of the Devonian sandstone sample (#ARG 09) were obtained for two very different zircon grains with lower eU-values are interpreted as detrital ages. Such old ages were not observed in other samples from the Sierras Australes. All samples from the west side of the SGW are characterized by significantly different AFT-ages. Whereas the eastern side revealed ages around 155 Ma the AFT-age of the Devonian sandstone sample (#ARG 09) taken close to the SGW on the west side is of 190.9 ± 14.8 Ma. The age of the Devonian sandstone indicates an earlier cooling of the west side of the SGW and might, therefore, represent east-directed thrust movement along the Sauce Grande wrench. Further to the west the Precambrian gneiss is characterized by an AFT-age of 242.7 ± 17.1 Ma, which is within error of ZHe-ages of three zircon grains. We interpret this similarity in age by fast cooling combined with a lower He-diffusion temperature of the zircon grains.

Applying the ZHe-age of the Upper Proterozoic ignimbrite (#ARG 07) a constant cooling model since about 350 Ma would represent the thermochronological age. The t-T model Please change Fig. 10 to Fig. 10A(Fig. 10) is only constraint by the ZHe-age.

Testing the geological evolution of the Devonian sandstone sample (#ARG 09) Please insert (Fig. 10C)against the thermochronological data set revealed a heating from surface temperature to a temperature of 180 °C at about 240 Ma. Assuming a surface temperature of about 15 °C and a geothermal gradient of 30 °C/km a Carboniferous and Permian sediment pile of about 5000 m could have overlain the Upper Devonian sandstone. The basin formation is followed by a fast cooling that reaches a temperature of about 65 °C at 200 Ma. Thereafter, nearly constant cooling to Quaternary surface temperature indicates exhumation of nearly 2000 m of rock cover. Similarly, the t-T evolution of the Proterozoic paragneiss (#ARG 08) Please insert (Fig. 10B).further to the west indicate a steady temperature increase, and, therefore, basin formation from near surface temperatures at Ordovician time to about 180 °C at the end of the Permian (250 Ma). The following rapid cooling is similar to the rapid cooling of the Devonian sandstone (#ARG 09) and changed at about 225 Ma to a constant cooling from 60 °C to surface temperature in the Upper Cenozoic. Comparing these two numerical models we have to state that the Late Permian to Triassic exhumation led to the erosion of about 3 km of Carboniferous to Permian rocks in the Sierras Australes, west of the SGWPlease change to Figs. 10A, 10B, 10C, Fig. 12). (Fig. 11).

4.4. Lopez Lecube intrusion

West of the Sierras Australes a porphyritic syntectonic syenite (ARG 05) of Permian emplacement age (around 258 ± 2 Ma; Pankhurst et al., 2006), revealed a ZHe-age of 246.4 ± 19.7 Ma, and AFT-age of 233.5 ± 17.0 Ma that indicate a fast cooling history during the Triassic and a slow cooling thereafter (AHe 134.5 ± 8.1 Ma)Please insert (Fig. 11).. The K/Ar cooling age of 245 ± 12 Ma, Rossello et al., 1997) of hornblende supports the fast cooling during the Triassic. The mean value of the c-axes corrected confined spontaneous fission-track length distribution of 13.4 ± 1.2 μm indicates a fast cooling below the PAZ. The t-T history (Fig. 26) point to extremely fast cooling in a very short time from > 350 °C at 260 Ma to 75 °C at about 250 Ma. During the Mesozoic, the temperature is nearly stable until 130 Ma. Thereafter, the cooling rate increases. Surface temperature might already be reached at 50 Ma. Assuming a palaeo-geothermal gradient of 30 °C/km and a surface palaeo-surface-temperature of 15 °C the temperature of 75 °C at 240 Ma might represent the temperature of the surrounding rocks and, therefore, indicate an intrusion depth of about 2I do not know why 2,000 m is wrong. Please leave in all cases throughout the whole manuscript the 2,000 m with a comma.000 m. The large K-feldspar crystals in a medium-grained matrix might point to a shallow intrusion depth as well.

5. Discussion: subsidence, inversion, and exhumation rates

The following chapter will translate the thermochronological data and the t-T evolution models into subsidence, and inversion history, and discuss the exhumation rates in selected time stepsPlease cite Table 7 here..

5.1. Ordovician to Permian (Gondwanides basin evolution and orogeny)

The Ordovician to Permian is characterized by the evolution of a sedimentary basin that overlaid the Precambrian metamorphic and intrusive basement in all areas. In Permian time, the sedimentary basin was deformed and partly metamorphosed. Within the Sierras Australes the SGW zone separates a western area with lower greenschist facies metasediments of Ordovician to Devonian age. The eastern side of the SGW zone is characterized by diagenetic to anchizonal Carboniferous to Permian sedimentary rocks.

The thermochronological data and the numerical modelling of samples from the Sierras Septentrionales indicate a Late Devonian to Early Carboniferous fast exhumation history (rate: 0.113 mm/a), which was followed by a subsidence with a rate of 0.019 mm/a (Fig. 12Please cite Table 7 here.). The exhumation led to the erosion of approximately 5.000 m rocks. Assuming a surface temperature of about 15 °C and a geothermal gradient of 30 °C/km (Zeil, 1980) and combining with the subsidence rate, the basin was filled again with about 2500 m of sedimentary rocks at the end of the Permian. At the same time, west of the Sauce Grande wrench subsidence with a rate of 0.024 mm/a leads also to the accumulation of 2500 m of sedimentary rocks. In the Permian, east of the SGW subsidence with a subsidence rate of 0.078 mm/a lead to the accumulation of nearly 3000 m of sedimentary rocks.

At the end of the Permian the Lopez Lecube syenite intruded the Precambrian metamorphic rocks and cooled extremely fast from

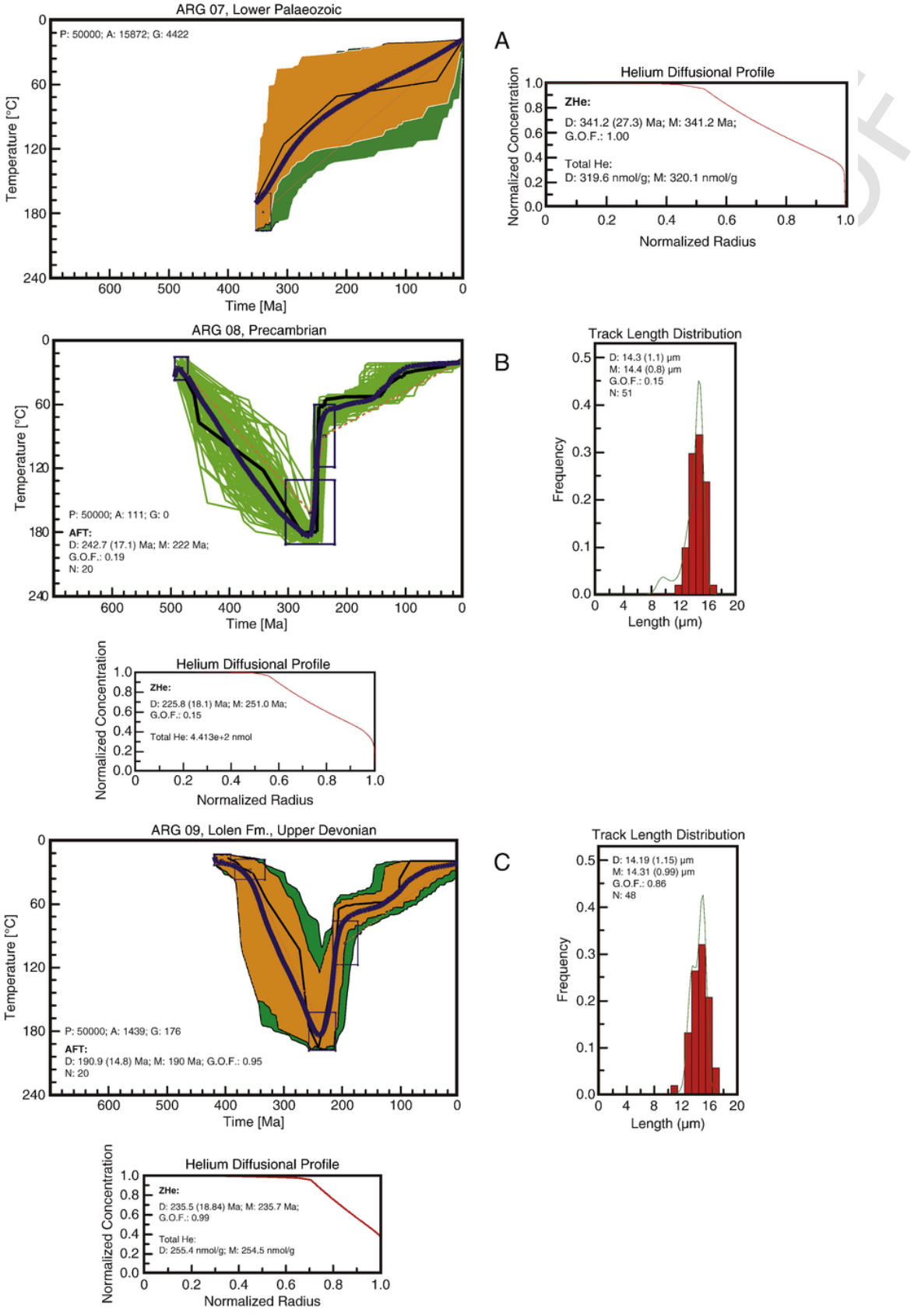
ARG 07, Lower Palaeozoic
P: 50000; A: 15872; G: 4422
Temperature [°C]
Time [Ma]
A
Helium Diffusional Profile
ZHe:
D: 341.2 (27.3) Ma; M: 341.2 Ma;
G.O.F.: 1.00
Total He:
D: 319.6 nmol/g; M: 320.1 nmol/g
Normalized Concentration
Normalized Radius
ARG 08, Precambrian
P: 50000; A: 111; G: 0
AFT:
D: 242.7 (17.1) Ma; M: 222 Ma;
G.O.F.: 0.19
N: 20
B
Track Length Distribution
D: 14.3 (1.1) µm
M: 14.4 (0.8) µm
G.O.F.: 0.15
N: 51
Frequency
Length (µm)
Helium Diffusional Profile
ZHe:
D: 225.8 (18.1) Ma; M: 251.0 Ma;
G.O.F.: 0.15
Total He: 4.413e+2 nmol
ARG 09, Lolen Fm., Upper Devonian
P: 50000; A: 1439; G: 176
AFT:
D: 190.9 (14.8) Ma; M: 190 Ma; G.O.F.: 0.95
N: 20
C
Track Length Distribution
D: 14.19 (1.15) µm
M: 14.31 (0.99) µm
G.O.F.: 0.86
N: 48
Helium Diffusional Profile
ZHe:
D: 235.5 (18.84) Ma; M: 235.7 Ma;
G.O.F.: 0.99
Total He:
D: 255.4 nmol/g; M: 254.5 nmol/g

magmatic temperature to about 75 °C within 10 Myr. We interpret the low temperature as an indication of the temperature of the Precambrian country rocks at the intrusion depth; indicating an intrusion depth of 2.000 to 3.000 m depending on the geothermal gradient in the area.

5.2. Permian to Jurassic (post Gondwanides)

The timing of the tectonic and erosion history of the western and the eastern side of the SGW is significantly different. During the Triassic, the west of the SWG (Fig. 12) exhumed rapidly (0.173 mm/a) causing the erosion of > 5.000 m of sedimentary rocks. The exhumation rate decreased significantly in the middle Triassic and continued with the same rate until the end of the Jurassic. During the whole Triassic east of the SGW subsidence continued with significantly increased rate (0.105 mm/a) leading to > 3.500 m of sedimentary rocks of Triassic age. Subsidence was finished at the end of the Triassic and changed to exhumation with a rate of 0.067 mm/a (erosion of > 3.000 m of sedimentary rocks) until the end of Jurassic. The spatial relationship between the strong exhumation of the western SGW and the strong subsidence of the eastern SWG points towards a sediment transport from west to east and, therefore, the western Sierras Australes as the source area of the sediments within the eastern Sierras Australes. Furthermore, the westerly dipping SGW thrust zone, might be an indication of tectonic induced subsidence of the eastern side due to the thrusting of the western area towards the east. The timing of the thrust movement is widely supposed to have occurred on Permian-Triassic transition (e.g. Tomezzoli and Vilas, 1999 and literature cited therein).

Testing the possible influence of Upper Jurassic magmatic activity in the Sierras Septentrionales as described for the adjacent Salado basin (Carol, 2010) leads to very different thermal histories for the Triassic and Jurassic. Without magmatic influence, it leads to a very low constant exhumation rate of 0.003 mm/a. If, however, magmatic activity has occurred a fast exhumation (rate of 0.030 mm/a) during the Lower and Middle Triassic is followed by a fast subsidence (rate of 0.033 mm/a) in Upper Triassic and Jurassic time.

A slow exhumation rate of 0.004 mm/a characterizes the exhumation history of the Lopez Lecube syenite during the Permian-Jurassic period.

5.3. Jurassic to recent (syn- and post-South Atlantic rift evolution)

This time interval is important for the evolution of the South Atlantic. Rifting is followed by post-rift formation of "passive margins". One aim of this thermochronological study was to evaluate the influence of the tectonic processes related to the opening, rift, and post-rift stage of the plate tectonic evolution of the South Atlantic. Considering all analysed samples from the area the exhumation history of the Sierras Septentrionales does not show any significant change in exhumation rate (about 0.015 mm/a). Similarly, east of the SGW the exhumation rates of about 0.015 mm/a are constant until the rocks reached the surface during the Quaternary. West of the SGW the Lower Cretaceous is characterized by an increase in exhumation rate from 0.004 mm/a (Jurassic) to 0.017 mm/a leading to the erosion of about 400 m of sedimentary rocks. Furthermore, the exhumation rate (0.015 mm/a) of the Lopez Lecube syenite increases as well.

During the Upper Cretaceous the sedimentation rates of the offshore part of the Colorado Basin is in the range of 0.125 mm/a (Loegering et al., 2013; Kuhlmann et al., 2010). Considering a lag time from erosion to sedimentation, it seems possible that the eastern area of the SGW in the Sierras Australes is a possible source for the sediments.

6. Conclusions

The above described thermochronological study clearly indicated that the rocks cropping out in the studied area have not been completely thermally reset (up to 300 °C) by the Upper Jurassic to Lower Cretaceous opening of the South Atlantic. The low-temperature thermochronological archives apatite and zircon still stored information on the pre-, syn-, and post-orogenic history of the Gondwanides in Argentina as well as on the Mesozoic and Cenozoic geological evolution related to the syn-, drift-, and post-rift stage of the South Atlantic. Therefore, the main issues can be answered as following:

1) What are the causes for the perpendicular trending of the mountain ranges in relation to the Argentine SAPCM? No significant crustal reorganization took place during the Mesozoic and Cenozoic. The NW-SE-trending mountain ranges received their geographic orientation during the syn- to post-orogenic history of the Gondwanides. Even the Mesozoic to Cenozoic Salado basin evolution follows this direction. Furthermore, the Upper Jurassic and Lower Cretaceous exhumation of the Sierras Septentrionales might have been caused by the "failed rift" evolution of the Salado basin and might, therefore, represent the "graben-shoulder".
2) Did the Argentine SAPCM ever evolved to a high-elevation margin during or shortly after the rifting stage? We do not see any evidence in the thermochronological data and the t-T evolution modelled.
3) If the Argentine SAPCM has had a high topography was it fast retreated or did it subside, thereafter? The determined LTT-data do not answer this question.
4) Did differentiated exhumation occur and is it controlled by pre-, syn-, and/or post-rift endogenic and exogenic forces. Yes, within our LTT-data we see differentiated exhumation. All those LTT-ages revealed form rocks taken from the same elevation on both sides of faults indicate forces acting during the syn- to drift-stage of the South Atlantic system. We cannot exclude the influence of significant climate changes during the Upper Cretaceous and Cenozoic on the exhumation history of the area.

Apart from the answers presented above the LTT-data provide further constrains on the timing of the movement of the major west-dipping thrust zone "Sauce Grande wrench" (SGW). It must have been active during the Permian and Triassic and caused exhumation of the western side and deposition on the eastern side. The top-to-the-east thrusting process might have induced the subsidence of the eastern side of the SGW. The major exhumation of the eastern side occurred later during the Jurassic and might have been the source area for the first sedimentation in the offshore Colorado and Salado basin. The Sierras Septentrionales might have been thermally influenced by magmatic activity during the Upper Jurassic. Lower Cretaceous syn-rift exhumation is only visible in the AFT-data set east of the

Fig. 10. A) t-T evolution model of ARG 07 with corresponding He-diffusional profile. B) t-T evolution of ARG 08 with corresponding length-distribution and He-diffusional profile. C) t-T evolution of ARG 09 with corresponding He-diffusional profile.

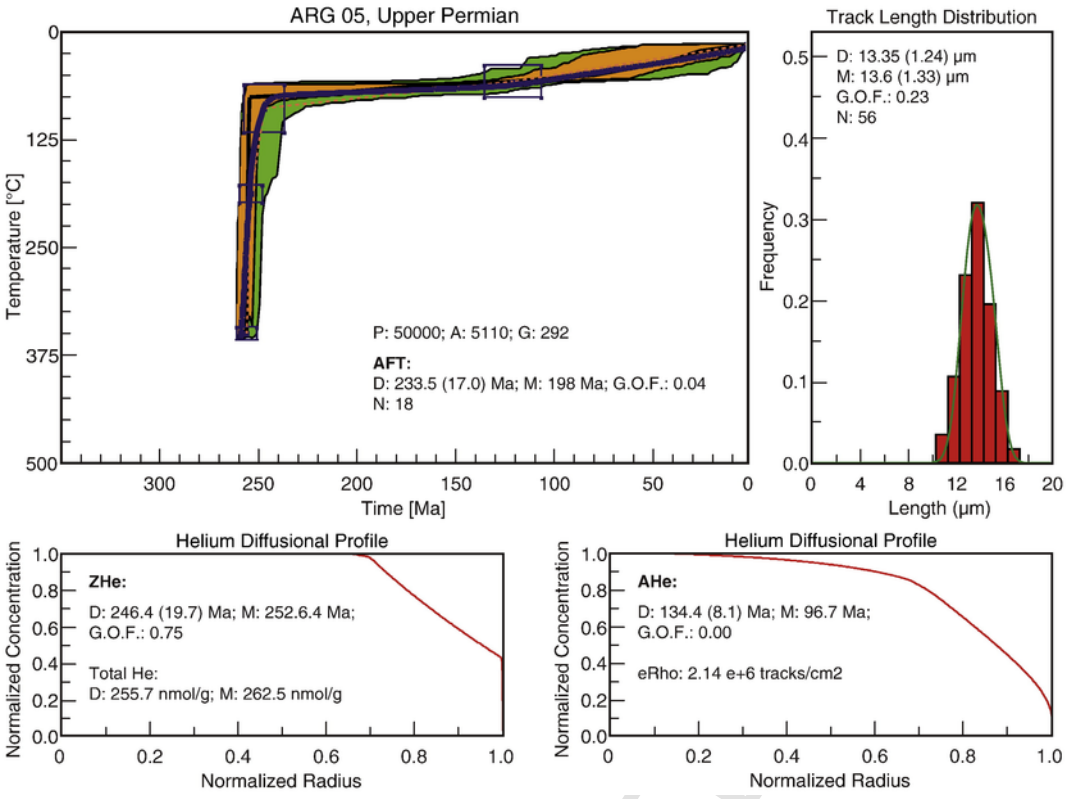

Fig. 11. t-T evolution of the Lopez Lecube Syenite (#ARG 05) with corresponding He-diffusional profile.

SGW. All exhumation rates are constant during the Cenozoic but vary related to the location of the samples.

Uncited references

Sutra ePlease take the uncited references out of the manuscript. Thank you.t al., 2013

Wagner and Reimer, 1972

Acknowledgements

We appreciate very much the discussions with members of the SPP-1375 SAMPLE. Furthermore, we like to thank Danny Stockli's team for the analytical assistance, Richard A. Ketcham and Raymond A. Donelick for providing the computer code HeFTy, Raymond A. Donelick for allowing us to use Dpar© as a kinetic factor, and Istvan Dunkl for providing the software code TrackKey. We also like to thank very much the reviewers Peter Kukla, Paul Green, Tim Redfield, Ana Olivia Barufi Franco-Magalhaes, and Claudio Gaucher for their constructive comments, and guiding suggestions.

In addition, we appreciate very much the technical support given by the Forschungs-Neutronenquelle FRM II at Garching, TU München, Germany organized by Dr. Gerstenberg.

Finally, without the financial support provided with grants to Ulrich A. Glasmacher by the German Research Foundation (Deutsche Forschungsgemeinschaft, DFG, GL182/14-1, 14-2) within the Priority Program 1375 (SAMPLE) and the DAAD (50753850) we would not be able to perform the research.

Table 6
Zircon fission-track data. U: uranium concentration in µg/g, n: number of counted grains, ρ_s: density of spontaneous tracks ($\times 10^5$/cm^2), N_s: number of spontaneous tracks, ρ_i: density of induced tracks ($\times 10^5$/cm^2), N_i: number of induced tracks, $P(\chi^2)$ is the probability that single grain ages are consistent and belong to the same population. Test is passed if $P(\chi^2) > 5\%$ (Galbraith, 1981). Ages calculated using a ζ-value of 123.00 (6.08) a/cm^2 for apatite, $N_d = 15.128$ tracks.

S.-No.	Elev. [m.a.s.l.]	Form. age	n	U ± std. [µg/g]	Sp. tracks		Ind. tracks		χ^2 [%]	Central age ± 1σ [Ma]
					ρ_s	N_s	ρ_i	N_i		
Sierras Australes										
East of Sauce Grande wrench										
ARG 17	416	Tunas Fm. Up. Perm.	17	175.3 ± 92.9	168.618	896	31.239	166	100.0	229.0 ± 22.5

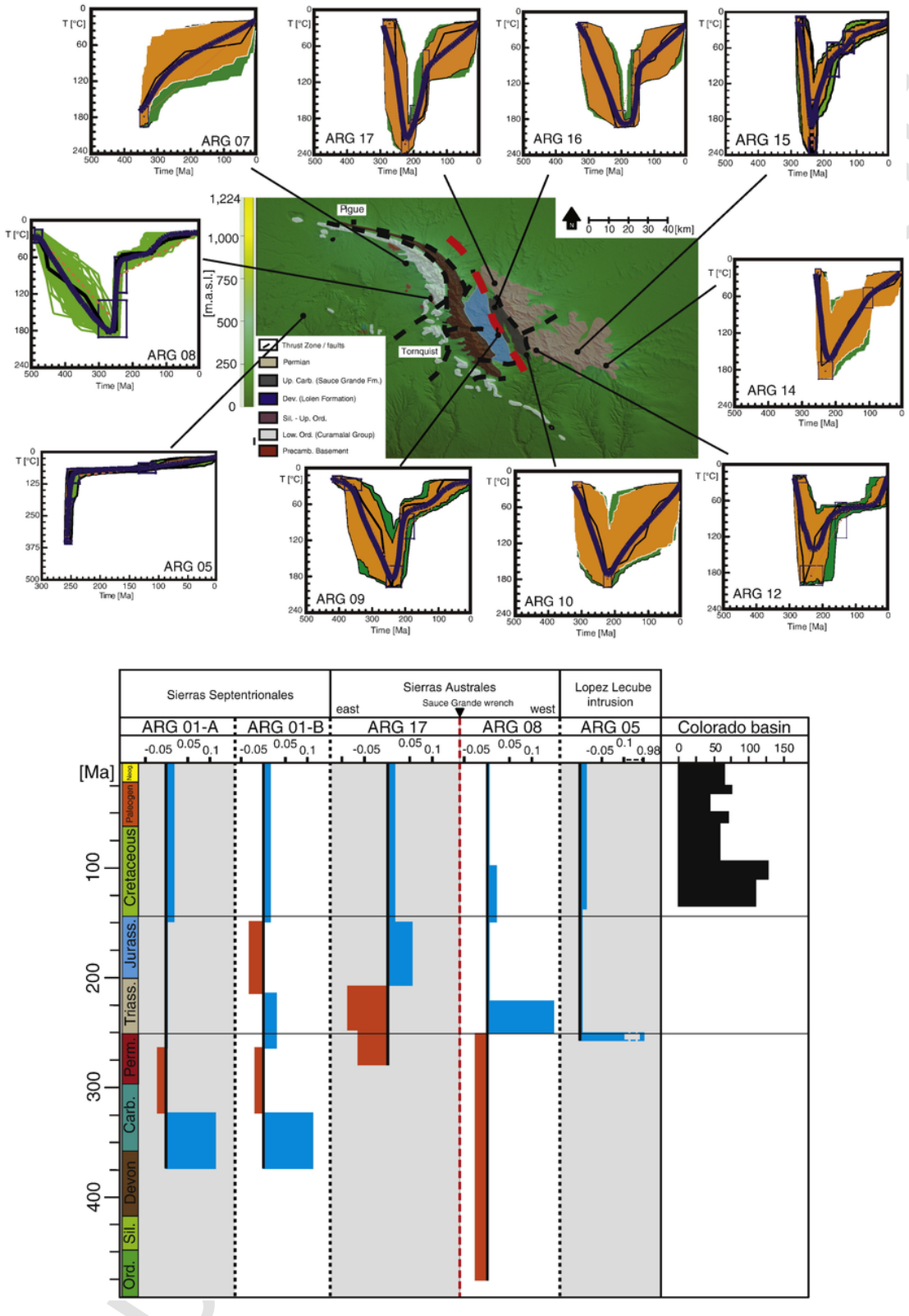

Fig. 12. A) Summary of the t-T evolution drawn on the geological map of the Sierras Australes (redrawn after Buggisch, 1987, Suero, 1972) that has been combined with the DEM-90 m. B) Calculated exhumation rates of five representative samples in comparison with published sedimentation rates from the Colorado basin (Loegering et al., 2013). Exhumation rates (calculated with a mean geothermal gradient of 30 °C/km) are given in mm/a, sedimentation rates are given in m/Ma. The dashed red line (between ARG 17 and ARG 08) represents the Sauce Grande wrench. (For interpretation of the references to colour in this figure legend, the reader is referred to the web version of this article.)

References

Alessandretti, L., Philipp, R.P., Chemale Jr., F., Brückmann, M.P., Zvirtes, G., Matte, V., Ramos, V.A., 2013. Provenance, volcanic record, and tectonic setting of the Paleozoic Ventania Fold Belt and the Claromecó Foreland Basin: implications on sedimentation and volcanism along the southwestern Gondwana margin. J. S. Am. Earth Sci. 47, 12–31.

Autin, J., Scheck-Wenderoth, M., Götze, H.-J., Reichert, C., Marchal, D., 2015. Deep structure of the Argentine margin inferred from 3D gravity and temperature modeling, Colorado Basin. Tectonophysics http://dx.doi.org/10.1016/j.tecto.2015.11.02.

Autin, J., Scheck-Wenderoth, M., Loegering, M.J., Anka, Z., Vallejo, E., 2013. Colorado Basin 3D structure and evolution, Argentine passive margin. Tectonophysics 604, 264–279.

Bauer, F.U., Glasmacher, U.A., Karl, M., Ring, U., Schumann, A., Nagudi, B., 2013. Tracing the exhumation history of the Rwenzori Mountains, Albertine Rift, Uganda, using low-temperature thermochronology. Tectonophysics 599, 8–28.

Bauer, F.U., Glasmacher, U.A., Malikwisha, M., Mambo, V.S., Mutete, B.V., 2010. The Eastern Congo – a beauty spot, rediscovered from a geological point of view. Geol. Today 26 (2) (March–April 2010).

Bauer, F.U., Glasmacher, U.A., Ring, U., Grobe, R.W., Mambo, V.S., Starz, M., 2015. Outline on the cooling history of the Albertine Rift, new evidence from the western rift shoulder, D.R. Congo. Int. J. Earth Sci. http://dx.doi.org/10.1007/s00531-015-1146-6.

Benedetto, J.L., 2010. El continente de Gondwana a través del tiempo. Una introducción a la Geología Histórica. Academia Nacional de Ciencias, Córdoba (384 pp.).

Bishop, P., 2007. Long-term landscape evolution: linking tectonics and surface processes. Earth Surf. Process. Landf. 32, 329–365.

Bracaccini, I.O., 1980. Cuenca del Salado. En J.C.M. Turner (Ed.) Segundo Simposio de Geología Regional Argentina. Academia Nacional de Ciencias de Córdoba, II: 879–918.

Braun, J., van der Beek, P., 2004. Evolution of passive margin escarpments: what can we learn from low-temperature thermochronology?. J. Geophys. Res. Earth Surf. 109 (F4) (2003–2012).

Braun, J., van der Beek, P., Batt, G., 2006. Quantitative Thermochronology: Numerical Methods for the Interpretation of Thermochronological Data. Cambridge University Press (ISBN-10: 0521830575).

Brix, M.R., Stockhert, B., Seidel, E., Theye, T., Thomson, S.N., Küster, M., 2002. Thermobarometric data from a fossil zircon partial annealing zone in high pressure–low temperature rocks of eastern and central Crete, Greece. Tectonophysics 349, 309–326.

Bushnell, D.C., Baldi, J.E., Bettini, F.H., Franzin, H., Kovas, E., Marinelli, R., Wartenburg, G.J., 2000. Petroleum systems analysis of the eastern Colorado Basin, offshore northern Argentina. Petroleum systems of South Atlantic margins. AAPG Mem. 73, 403–415.

Carlson, W.D., Donelick, R.A., Ketcham, R.A., 1999. Variability of apatite fission-track annealing kinetics: I. Experimental results. Am. Mineral. 84, 1213–1223.

Carol, E., Kruse, E., Pousa, J., 2010. Eco-hydrological role of deep aquifers in the Salado sedimentary basin in the Province of Buenos Aires, Argentina. Environ. Earth Sci. 60, 749–756.

Cingolani, C.A., 2011. The Tandilia System of Argentina as a southern extension of the Rio de la Plata craton: an overview. Int. J. Earth Sci. 100, 221–242.

Cobbold, P.R., Massdbie, A.C., Rossello, E.A., 1986. Hercynian wrenching and thrusting in the Sierras Australes foldbelt, Argentina. Hercynica 2, 135–148.

Cogné, N., Gallagher, K., Cobbold, P.R., Riccomini, C., Gautheron, C., 2012. Post break-up tectonics in southeast Brazil from thermochronological data and combined inverse forward thermal history modeling. J. Geophys. Res. 117, B11413.

Crovetto, C.B., Novara, I.L., Introcaso, A., 2007. A stretching model to explain the Salado basin (Argentina). Bol. Inst. Fisiog. Geol. 77.

D'Angiola, M., Echeveste, H.J., Risi, D., Vinciguerra, P., 1992. Analisisestructural de la faja milonıtica del flanco norte del Cerro Albion, Sierras de Tandil. In: Prov. de Buenos Aires. Jornadas Geologicas Bonaerenses, Vol. 3, pp. 63–67.

Dalla Salda, L.H., 1975. Geologia y petrologia del basamento cristalino en el area del Cerro El Cristo e Isla Martın Garcıa. Provincia de Buenos Aires, Republica Argentina (Tesis doctoral). Facultad de Ciencias Naturales y Museo. Univ. Nacional de La Plata.

Dávila, F.M., Lithgow-Bertelloni, C., 2013. Dynamic topography in South America. J. S. Am. Earth Sci. 43, 127–144.

Dodson, M.H., 1973. Closure temperature in cooling geochronological and petrological systems. Contrib. Mineral. Petrol. 40, 259–274.

Donelick, R.A., 1993. A method of fission track analysis utilizing bulk chemical etching of apatite. Patent number 5,267,274, USA.

Donelick, R.A., 1995. A method of fission track analysis utilizing bulk chemical etching of apatite. Patent number 658,800, Australia.

Donelick, R.A., Ketcham, R.A., Carlson, W.D., 1999. Variability of apatite fission track annealing kinetics II: crystallographic orientation effects. Am. Mineral. 84, 1224–1234.

Donelick, R.A., O'Sullivan, P.B., Ketcham, R.A., 2005. Apatite fission-track analysis. In: Reiners, P.W., Ehlers, T.A. (Eds.), Low-Temperature Thermochronology: Techniques, Interpretations, and Applications: Rev. Mineral. Geochem, Vol. 58, pp. 49–94.

Dunkl, I., 2002. Trackkey: a Windows program for calculation and graphical presentation of fission track data. Comput. Geosci. 28, 3–12.

Farley, K.A., 2002. (U-Th)/He dating: techniques, calibrations, and applications. Rev. Mineral. Geochem. 47, 819–844.

Farley, K.A., 2000. Helium diffusion from apatite: general behaviour as illustrated by Durango fluorapatite. J. Geophys. Res. Solid Earth 105, 2903–2914.

Farley, K.A., 2007. He diffusion systematics in minerals: evidence from synthetic monazite and zircon structure phosphates. Geochim. Cosmochim. Acta 71, 4015–4024.

Farley, K.A., Wolf, R.A., Silver, L.T., 1996. The effects of long alpha-stopping distances on (U-Th)/He ages. Geochim. Cosmochim. Acta 60, 4223–4229.

Flowers, R.M., Shuster, D.L., Wernicke, B.P., Farley, K.A., 2007. Radiation damage control on apatite (U–Th)/He dates from the Grand Canyon region, Colorado Plateau. Geology 35, 447–450.

Flowers, R.M., Ketcham, R., Shuster, D.L., Farley, K.A., 2009. Apatite (U/Th)/He thermochronometry using a radiation damage accumulation and annealing model. Geochim. Cosmochim. Acta 73, 2347–2365.

Franco-Magalhães, A.O.B., Hackspacher, P.C., Glasmacher, U.A., Saad, A.R., 2010. Rift to post-rift evolution of a "passive" continental margin: the Ponta Grossa Arch, SE Brazil. Int. J. Earth Sci. 99, 1599–1613.

Franke, D., Neben, S., Ladage, S., Schreckenberger, B., Hinz, K., 2007. Margin segmentation and volcano-tectonic architecture along the volcanic margin of Argentina/Uruguay, South Atlantic. Mar. Geol. 244, 46–67.

Fryklund, B., Marshall, A., Stevens, J., 1996. Cuenca del Colorado. In: Ramos, V.A., Turic, M.A. (Eds.), Geología y recursos naturales de la Plataforma Continental Argentina. Relatorio del XIII° Congreso Geológico Argentino y III° Congreso de Exploración de Hidrocarburos, Buenos Aires pp. 135–158.

Galbraith, R.F., 1981. On statistical models for fission track counts. Math. Geol. 13 (6), 471–478.

Gallagher, K., Brown, R.W., Johnson, C., 1998. Fission track analysis and its application to geological problems. Annu. Rev. Earth Planet. Sci. 26, 519–572.

Garver, J.I., 2002. Discussion: metamictization of natural zircon: accumulation versus thermal annealing of radioactivity-induced damage. Contrib. Mineral. Petrol. 143, 756–757.

Garver, J.I., Kamp, P.J.J., 2002. Integration of zircon color and zircon fission track zonation patterns in orogenic belts: application of the Southern Alps, New Zealand. Tectonophysics 349, 203–219.

Gaucher, C., Finney, S.C., Poiré, D.G., Valencia, V.A., Grove, M., Blanco, G., Pamoukaghliá, K., Gómez Peral, L., 2008. Detrital zircon ages of Neoproterozoic sedimentary successions in Uruguay and Argentina: insights into the geological evolution of the Rio de la Plata Craton. Precambrian Res. 167, 150–170. http://dx.doi.org/10.1016/j.precamres. 2008.07.006.

Green, P.F., 1981. 'Track-in track' length measurements in annealed apatites. Nucl. Tracks 5, 121–128.

Green, P.F., 1988. The relationship between track shortening and fission track age reduction in apatite: combined influences of inherent instability, annealing anisotropy, length bias and system calibration. Earth Planet. Sci. Lett. 89 (3–4), 335–352.

Green, P.F., Durrani, S.A., 1977. Annealing studies of tracks in crystals. Nucl. Track Detect. 1, 33–39.

Green, P.F., Duddy, I.R., Gleadow, A.J.W., Tingate, P.R., Laslett, G.M., 1986. Thermal annealing of fission tracks in apatite, 1. A qualitative description. Chem. Geol. Isot. Geosci. 59, 237–253.

Green, P.F., Lidmar-Bergström, K., Japsen, P., Bonow, J.M., Chalmers, J.A., 2013. Stratigraphic landscape analysis, thermochronology and the episodic development of elevated, passive continental margins. Geol. Surv. Den. Greenl. 30.

Grist, A.M., Ravenhurst, C.E., 1992. Mineral separation techniques used at Dalhousie University. In: Zentilli, M., Reynolds, P.H. (Eds.), Short Course Handbook on Low Temperature Thermochronology. Mineral Associ. Can. Short Course Handb, Vol. 2, pp. 203–209 (20 Append.).

Grist, A.M., Ravenhurst, C.E., 1992. A step-by-step laboratory guide to fission track thermochronology at Dalhousie University. In: Zentilli, M., Reynolds, P.H. (Eds.), Short Course Handbook on Low Temperature Thermochronology. Mineral Associ. Can. Short Course Handb, Vol. 1, pp. 190–201 (20 Append.).

Guenthner, W.R., Barbeau, D.L., Reiners, P.W., Thomson, S.N., 2010. Slab window migration and terrane accretion preserved by low-temperature thermochronology of a magmatic arc, northern Antarctic Peninsula. Geochem. Geophys. Geosyst. 11. http://dx.doi.org/10.1029/2009GC002765.

Guenthner, W.R., Reiners, P.W., Ketcham, R.A., Nasdala, L., Giester, G., 2013. Helium diffusion in natural zircon: radiation damage, anisotropy, and the interpretation of zircon (U-Th)/He thermochronology. Am. J. Sci. 313, 145–198.

Harrington, H.J., 1955. The Permian Eurydesma fauna of eastern Argentina. J. Paleontol. 29, 112–128.
Hartmann, L.A., Santos, J.O.S., Cingolani, C.A., McNaughton, N.J., 2002. Two Paleoproterozoic orogenies in the evolution of the Tandilia Belt, Buenos Aires, as evidenced by zircon U-Pb SHRIMP geochronology. Int. Geol. Rev. 44, 528–543. http://dx.doi.org/10.2747/0020-6814.44.6.528.
Hiruma, S.T., Riccomini, C., Modenesi-Gauttieri, M.C., Hackspacher, P.C., Neto, J.C.H., Franco-Magalhaes, A.O.B., 2010. Denudation history of the Bocaina Plateau, Serra do Mar, southeastern Brazil: relationships to Gondwana breakup and passive margin development. Gondwana Res. 18, 674–687.
Huismans, R.S., Beaumont, C., 2002. Asymmetric lithospheric extension: the role of frictional-plastic strain softening inferred from numerical experiments. Geology 30, 211–214.
Huismans, R.S., Beaumont, C., 2003. Symmetric and asymmetric lithospheric extension: relative effects of frictional-plastic and viscous strain softening. J. Geophys. Res. 108, 2496. http://dx.doi.org/10.1029/2002JB002026.
Huismans, R.S., Beaumont, C., 2007. Roles of lithospheric strain softening and heterogeneity in determining the geometry of rifts and continental margins. In: Karner, G.D., Manatschal, G., Pinhiero, L.M. (Eds.), Imaging, Mapping and Modelling Continental Lithosphere Extension and Breakup 107–134. Geological Society, London, Special Publications, Vol. 282. http://dx.doi.org/10.1144/SP282.6.
Huismans, R.S., Beaumont, C., 2008. Complex rifted continental margins explained by dynamical models of depth-dependent lithospheric extension. Geology 36, 163–166. http://dx.doi.org/10.1130/G24231A.1.
Huismans, R.S., Beaumont, C., 2011. Depth-dependent extension, two-stage breakup and cratonic underplating at rifted margins. Nature 473. http://dx.doi.org/10.1038/nature 09988.
Huismans, R.S., Beaumont, C., 2014. Contrasting characteristics of rifted continental margins explained by depth-dependent lithospheric extension: effects of detachment and strong and weak lower crust. Earth Planet. Sci. Lett. 248, 315–324.
Hurford, A.J., 1986. Standardization of fission track dating calibration: results of questionnaire distributed by international union of geological sciences subcommission on geochronology. Nucl. Tracks Radiat. Meas. 11, 329–333.
Hurford, A.J., 1990. Standardization of fission track dating calibration: recommendation by the fission track working group of the I.U.G.S. Subcommission on geochronology. Chem. Geol. 80, 171–178.
Hurford, A.J., Green, P.F., 1982. A user's guide to fission-track dating calibration. Earth Planet. Sci. Lett. 59, 343–354.
Hurford, A.J., Green, P.F., 1983. The zeta age calibration of fission-track dating. Isot. Geosci. 1, 285–317.
Introcaso, A., Ramos, V., 1984. La cuenca del Salado: un modelo de evolución aulacogénica. In: IX Congreso Geológico Argentino, Actas III, 27–46. Bariloche.
Japsen, P., Bonow, J.M., Green, P.F., Chalmers, J.A., Lidmar-Bergström, K., 2006. Elevated, passive continental margins: long-term highs or Neogene uplifts? New evidence from West Greenland. Earth Planet. Sci. Lett. 248, 315–324.
Karl, M., Glasmacher, U.A., Kollenz, S., Franco-Magalhaes, A.O.B., Stockli, D.F., Hackspacher, P., 2013. Evolution of the South Atlantic passive continental margin in southern Brazil derived from zircon and apatite (U–Th–Sm)/He and fission-track data. Tectonophysics 604, 224–244.
Keidel, J., 1913. Über das Alter, die Verbreitung und die gegenseitigen Beziehungen der verschiedenen tektonischen Strukturen in den argentinischen Gebirgen. In: 12° Session du Congrés Géologique International (Toronto). Compte Rendus pp. 671–687.
Keidel, J., 1916. La geología de las Sierras de la Provincia de Buenos Aires y sus relaciones con las montañas de Sudáfrica y Los Andes. In: Ministerio de Agricultura de la Nación, Sección Geología, Mineralogía y Minería, Anales, Vol. 11, pp. 1–78.
Keidel, J., 1921. Sobre la distribución de los depósitos glaciares del Pérmico conocidos en la Argentina y su significación para la estratigrafía de la serie del Gondwana y la paleogeografía del Hemisferio Austral. Acad. Nac. Cienc. Bol. 25, 239–368.
Ketcham, R.A., 2005. Forward and inverse modelling of low-temperature thermochronometry data. Rev. Mineral. Geochem. 58, 275–314.
Ketcham, R.A., 2009. HeFTy Version 1.6.7, Manual.
Ketcham, R.A., Carter, A., Donelick, R.A., Barbarand, J., Hurford, A.J., 2007. Improved modeling of fission-track annealing in apatite. Am. Mineral. 92, 789–798.
Ketcham, R.A., Carter, A., Donelick, R.A., Barbarand, J., Hurford, A.J., 2007. Improved measurement of fission-track annealing in apatite using c-axis projection. Am. Mineral. 92, 789–798.
Ketcham, R.A., Donelick, R.A., Balestrieri, M.L., Zattin, M., 2009. Reproducibility of apatite fission-track length data and thermal history reconstruction. Earth Planet. Sci. Lett. 284, 504–515.
Kooi, H., Beaumont, C., 1994. Escarpment evolution on high-elevation rifted margins: insights derived from a surface process model that combines diffusion, advection, and reaction. J. Geophys. Res. 99, 12191–12209.
Kooi, H., Beaumont, C., 1996. Large-scale geomorphology: classical concepts reconciled and integrated with contemporary ideas via a surface process model. J. Geophys. Res. 101, 3361–3386.
Kostadinoff, J., 1993. Geophysical evidence of a Paleozoic basin in the interhilly area of Buenos Aires Province, Argentina. In: Congr. Internat. Strat. et Geol. du Carbonifere et Permien, Comptes Rendus XII, ICC-P, Vol. 1, pp. 397–404.
Kostadinoff, J., Font, G., 1985. Cuenca interserrana bonaerense, Argenting. V. Congr. Latinoam. Geol. 4, 105–121.
Kuhlmann, G., Adams, S., Campher, C., van der Spuy, D., di Primio, R., Horsfield, B., 2010. Passive margin evolution and its controls on natural gas leakage in the southern Orange Basin, blocks 3/4, offshore South Africa. Mar. Pet. Geol. 27, 973–992.
Kusznir, N.J., Ziegler, P.A., 1992. The mechanics of continental extension and sedimentary basin formation: a simple-shear/pure-shear flexural cantilever model. Tectonophysics 215, 117–131.
Kusznir, N.J., Karner, G.D., Egan, S., 1987. Geometric, thermal and isostatic consequences of detachments in continental lithosphere extension and basin formation. In: Beaumont, C., Tankard, A.J. (Eds.), Sedimentary Basins and Basin Forming Mechanisms. Mem. Can. Soc. Petrol. Geol, Vol. 12, pp. 185–203.
Laslett, G.M., Gleadow, A.J.W., Duddy, I.R., 1984. The relationship between fission track length and track density in apatite. Nucl. Tracks 9, 29–37.
Laslett, G.M., Green, P.F., Duddy, I.R., Gleadow, A.J.W., 1987. Thermal annealing of fission tracks in apatite: 2 - a quantitative analysis. Chem. Geol. Isot. Geosci. 65, 1–13.
Lisker, F., Ventura, B., Glasmacher, U.A., 2009. Apatite thermochronology in modern geology. Geol. Soc. Lond. Spec. Publ. 324, 1–23.
Loegering, M.J., Anka, Z., Autin, J., di Primio, R., Marchal, D., Rodriguez, J.F., Franke, D., Vallejo, E., 2013. Tectonic evolution of the Colorado Basin, offshore Argentina, inferred from seismo-stratigraphy and depositional rates analysis. Tectonophysics 604, 245–263.
Lopez-Gamundi, O.R., Rossello, E.A., 1998. Basin fill evolution and paleotectonic patterns along the Samfraugeosyncline: the Sauce Grande basin–Ventana foldbelt (Argentina) and Karoo basin–Cape foldbelt (South Africa) revisited. Geol. Rundsch. 86, 819–834.
McKenzie, D.P., 1978. Some remarks on the development of sedimentary basins. Earth Planet. Sci. Lett. 40, 25–32.
Mitchell, S.G., Reiners, P.W., 2003. Influence of wildfires on apatite and zircon (U-Th)/He ages. Geology 31, 1025–1028.
Nasdala, L., 2009. Pb^{+} irradiation of synthetic zircon ($ZrSiO_4$): infrared spectroscopic investigation - discussion. Am. Mineral. 94, 853–855.
Ollier, C.D., 1985. Morphotectonics of continental margins with great escarpments. In: Morisawa, M., Hack, J.T. (Eds.), Tectonic Geomorphology. Allen and Unwin, Boston, pp. 3–25.
Osmundsen, P.T., Redfield, T.F., 2011. Crustal taper and topography at passive continental margins. Terra Nova 00, 1–13.
Pángaro, F., Ramos, V.A., 2012. Paleozoic crustal blocks of onshore and offshore central Argentina: new pieces of the southwestern Gondwana collage and their role in the accretion of Patagonia and the evolution of Mesozoic south Atlantic sedimentary basins. Mar. Pet. Geol. 37, 162–183.
Pankhurst, R.J., Rapela, C.W., Fanning, C.M., Márquez, M., 2006. Gondwanide continental collision and the origin of Patagonia. Earth Sci. Rev. 76, 235–257.
Perez-Diaz, L., Eagles, G., 2014. Constraining South Atlantic growth with seafloor spreading data. Tectonics 33, 1848–1873.
Poiré, D.G., Gaucher, C., 2009. Lithostratigraphy. Neoproterozoic-Cambrian evolution of the Ri'o de la Plata Palaeocontinent. In: Gaucher, C., Sial, A.N., Halverson, G.P., Frimmel, H.E. (Eds.), Neoproterozoic-Cambrian Tectonics, Global Change and Evolution: A Focus on Southwestern Gondwana. Developments in Precambrian Geology. vol. 16. Elsevier, pp. 87–101. http://dx.doi.org/10.1016/S0166-2635(09)01605-3 (4.2).
Poiré, D.G., Spalletti, L.A., del Valle, A., 2003. The Cambrian Ordovician siliciclastic platform of the Balcarce Formation (Tandilia System, Argentina): facies, trace fossils, palaeoenvironments and sequence stratigraphy. Geol. Acta 1, 41–60.
Rahn, M.K., Brandon, M.T., Batt, G.E., Garver, J.I., 2004. A zero-damage model for fission-track annealing in zircon. Am. Mineral. 89, 473–484.
Ramos, V.A., Chemale, F., Naipauer, M., Pazos, P.J., 2013. A provenance study of the Paleozoic Ventania system (Argentina): transient complex sources from western and eastern Gondwana. Gondwana Res. 26, 719–740.
Rapela, C.W., Pankhurst, R.J., Casquet, C., Fanning, C.M., Baldo, E.G., Gonzalez-Casado, J.M., Galindo, C., Dahlquist, J., 2007. The Rio de la Plata craton and the assembly of SW Gondwana. Earth Sci. Rev. 83, 49–82.
Rapela, C.W., Pankhurst, R.J., Fanning, C.M., Grecco, L.E., 2003. Basement evolution of the Sierra de la Ventana Fold Belt: new evidence for Cambrian continental rifting along the southern margin of Gondwana. J. Geol. Soc. 160, 613–628.
Reiners, P.W., 2005. Zircon (U-Th)/He thermochronometry. Rev. Mineral. Geochem. 58, 151–179.
Reiners, P.W., Farley, K.A., 2001. Influence of crystal size on apatite (U-Th)/He thermochronology: an example from the Bighorn Mountains, Wyoming. Earth Planet. Sci. Lett. 188, 413–420.

Reiners, P.W., Farley, K.A., Hickes, H.J., 2002. He diffusion and (U-Th)/He thermochronometry of zircon: initial results from Fish Canyon Tuff and Gold Butte, Nevada. Tectonophysics 349, 297–308.

Reiners, P.W., Spell, T.L., Nicolescu, S., Zanetti, K.A., 2004. Zircon (U-Th)/He thermochronometry: He diffusion and comparisons with $^{40}Ar/^{39}Ar$ dating. Geochim. Cosmochim. Acta 68, 1857–1887.

Rossello, E.A., Massabie, A.C., Lopez-Gamundi, O.R., Cobbold, P.R., Gapais, D., 1997. Late Paleozoic transpression in Buenos Aires and northeast Patagonia ranges, Argentina. J. S. Am. Earth Sci. 10, 389–402.

Sacek, V., Braun, J., van der Beek, P., 2012. The influence of rifting on escarpment migration on high elevation passive continental margins. J. Geophys. Res. Solid Earth 117 (B4).

Shuster, D.L., Farley, K.A., 2009. The influence of artificial radiation damage and thermal annealing on helium diffusion kinetics in apatite. Geochim. Cosmochim. Acta 73 (1), 183–196.

Shuster, D.L., Flowers, R.M., Farley, K.A., 2006. The influence of natural radiation damage on helium diffusion kinetics in apatite. Earth Planet. Sci. Lett. 249, 148–161.

Sobel, E.R., Seward, D., 2010. Influence of etching conditions on apatite fission-track etch pit diameter. Chem. Geol. 271, 59–69.

Suero, T., 1972. Compilaci6n geol6gica de las Sierras Australes de la provincia de Buenos Aires. LEMIT (La Plats) (4,1&r. 3. I35 147).

Summerfield, M.A. (Ed.), 2000. Geomorphology and Global Tectonics. Wiley, Chichester (386 pp.).

Sutra, E., Manatschal, G., Mohn, G., Unternehr, P., 2013. Quantification and restoration of extensional deformation along the Western Iberia and Newfoundland rifted margins. Geochem. Geophys. Geosyst. 14, 2575–2597. http://dx.doi.org/10.1002/ggge.20135.

Tomezzoli, R.N., 2001. Further palaeomagnetic results from the Sierras Australes fold and thrust belt, Argentina. Int. J. Geophys. 147, 356–366.

Tomezzoli, R.N., Vilas, J.F., 1999. Palaeomagnetic constraints on the age of deformation of the Sierras Australes thrust and fold belt, Argentina. Int. J. Geosci. 138, 857–870.

Vayssaire, A., Prayitno, W., Figueroa, D., Quesada, S., 2007. Petroleum systems of Colorado and Malvinas Basins, deep water Argentina, South Atlantic petroleum systems. Geol. Soc. London, London, 10.

Vermeesch, P., Seward, D., Latkoczy, C., Wipf, M., Gunther, D., Baur, H., 2007. Alpha-emitting mineral inclusions in apatite, their effect on (U–Th)/He ages, and how to reduce it. Geochim. Cosmochim. Acta 31, 1737–1746.

Von Gosen, W., Buggisch, W., Dimierz, L.V., 1990. Structural and metamorphic evolution of the Sierras Australes (Buenos Aires province, Argentina). Geol. Rundsch. 79 (3), 797–821.

Von Gosen, W., Buggisch, W., Krumm, S., 1991. Metamorphism and deformation mechanisms in the Sierras Australes fold and thrust belt (Buenos Aires Province, Argentina). Tectonophysics 185, 335–356.

Wagner, G.A., Reimer, G.M., 1972. Fission-track tectonics: the tectonic interpretation of fission track apatite ages. Earth Planet. Sci. Lett. 14, 263–268.

Wagner, G.A., van den Haute, P., 1992. Fission Track Dating. Kluwer Verlag, Enke Publisher (285 pp.).

Wernicke, B., 1985. Uniform-sense normal simple shear of the continental lithosphere. Can. J. Earth Sci. 22, 108–125.

Wolf, R.A., Farley, K.A., Silver, L.T., 1996. Helium diffusion and low-temperature thermochronometry of apatite. Geochim. Cosmochim. Acta 60, 4231–4240.

Yamada, R., Tagami, T., Nishimura, S., Ito, H., 1995. Annealing kinetics of fission tracks in zircon: an experimental study. Chem. Geol. Isot. Geosci. 122, 249–258.

Zambrano, J.J., 1974. Cuencas Sedimentarias en el subsuelo de la provincia de Buenos Aires y zonas adyacentes. Rev. Asoc. Geol. Argent. 29 (4), 443–449.

Zambrano, J.J., Urien, C.M., 1970. Geological outline of the basins in southern Argentina and their offshore extension. J. Geophys. Res. 75 (8), 1363–1396.

Zeil, W., 1980. Brinkmanns Abriß der Geologie, erster Band: Allgemeine Geologie. 12. Auflage. Ferdinand Enke Verlag, Stuttgart. ISBN: 3-432-80592-6.

Ziegler, P.A., Cloetingh, S., 2004. Dynamic processes controlling evolution of rifted basins. Earth Sci. Rev. 64, 1–50.

Zimmermann, U., Poire, D.G., Gomez Peral, L., 2011. Neoproterozoic to lower Palaeozoic successions of the Tandilia system in Argentina: implication for the palaeotectonic framework of southwest Gondwana. Int. J. Earth Sci. 100, 489–510.